



ÉCOLE
POLYTECHNIQUE
DE BRUXELLES



UNIVERSITÉ LIBRE DE BRUXELLES

Interferometric stabilisation of a fibre-based optical computer

Experimental study

Mémoire présenté en vue de l'obtention du diplôme
d'Ingénieur Civil physicien à finalité spécialisée

Denis Verstraeten

Directeur

Professeur Marc Haelterman

Co-Promoteur

Professeur Serge Massar

Superviseur

Lorenz Butschek

Service

Opera

Année académique
2018 - 2019

Abstract

Reservoir computing is a recent computing paradigm based on the concept of recurrent neural network that reaches state of the art performances in time-dependent data processing. The mathematical description of this computation scheme imposes so little constraints that it can be implemented on physical systems such as optical setups. A novel fibre-based reservoir computer relying on wavelength division multiplexing of the neurons is presented. It is supposed to exhibit an increased data processing rate compared to the previous generation of photonic reservoir computers based on time division multiplexing. In the new scheme proposed, the reservoir is physically implemented by an optical cavity and the coupling between the neurons is performed by an intra-cavity phase modulator. In order for the reservoir computer to work properly, the cavity has to be stabilised. To do so, an analytical model for the transfer function of the cavity is derived and validated by comparison with experimental curves and the Pound-Drever-Hall technique, which is an advanced cavity stabilisation scheme, is implemented. The cavity is characterised experimentally by finding the Pound-Drever-Hall settings that minimise the phase noise in order to ultimately improve the performance of the reservoir computer.

Keywords: Reservoir computing, neural network, machine learning, photonic reservoir computing, ring cavity, cavity stabilisation, interferometric stabilisation, Pound-Drever-Hall technique

Acknowledgements

First, I would like to thank my promoters for giving me the opportunity to do my master thesis on such an interesting topic, and for sharing their knowledge and experience with me. I have learned more from this work than I have from any other courses that I have followed during my cursus (except *Physique Générale* maybe...). I am grateful to Marc Haelterman for considering me as legitimate PhD candidate and for showing me what were the humane qualities that make a good scientist. I would also like to thank Serge Massar for his advice, his reactivity to answer my questions and for the last minute review of the thesis that he did. Many thanks to Lorenz Butschek without whom this thesis would not exist. Thank you for all the time you spent with me in the lab, for your patience when you were explaining (sometimes very basic) things, for the very careful rereading of the thesis that you did in last minute, and for your ability to decode my English which can get sometimes quite approximative. Once again, a big thank you for all of this. Before leaving the academics to move on to more personal acknowledgments, I would like to thank Michel Kinnaert who accepted to meet me twice throughout the year and with whom I passionately discussed the stabilisation issues encountered. I would finally like to thank my readers for the time they will invest in my work. I hope you will enjoy it. It is now time to thank my closest ones. First, I would like to thank my parents for giving me the opportunity to pursue higher education. Going to university is a privilege that is too often forgotten, and I am thankful they offered me this chance. Finally, I want to thank by biggest support of all, Cassandra. During this year, she shared my ups, and helped me during the downs, she always knew how to cheer me up when the work was not progressing the way I wanted. Thank you for being the amazing person that you are.

Contents

1	Introduction	7
2	Reservoir Computing	9
2.1	Reservoir Computing framework	9
2.1.1	Artificial Neural Network	9
2.1.2	Reservoir Computing	10
2.1.3	Machine Learning	10
2.2	Mathematical Model	11
2.2.1	Dynamics of the reservoir	11
2.2.2	Computation of the output weights	13
2.3	Introduction to Photonic Reservoir Computing	13
2.3.1	Time Division Multiplexing of the neurons	14
2.3.2	Simplifying assumptions	14
2.3.3	Neurons encoded in light intensity	16
2.3.4	Neurons encoded in phaser representation of the electric field	16
2.3.5	Simulations	17
3	Photonic Reservoir Computer with Wavelength Division Multiplexed neurons	20
3.1	Description of the scheme	20
3.1.1	Working principle	21
3.1.2	Frequency coupling of the neurons	22
3.1.3	Mathematical model	23
4	Interferometric stabilisation of reservoir cavity	26
4.1	Introduction	26
4.1.1	Fabry-Perot interferometer	26
4.1.2	Ring cavity	28
4.1.3	Interferometric properties of the reservoir cavity	28
4.2	Experimental setup	30
4.3	Characterisation of the reservoir	32
4.3.1	Transfer function of the cavity	32
4.3.2	Effective losses	36
4.3.3	Modulation depth	38
4.4	Pound-Drever-Hall stabilisation technique	39
4.4.1	Introduction	39
4.4.2	Pound-Drever-Hall scheme	41
4.4.3	Pound-Drever-Hall technique for the reservoir	44
4.5	Characterisation of the stabilisation performance for different regimes	44
4.5.1	Approach	45
4.5.2	Results	52

5	Conclusion	55
A	Experimental results	57
B	Specifications	65
	Acronyms	66

Chapter 1

Introduction

Today’s industrialised society has been vastly shaped by information and communication technologies and the demand for always faster data processing rates is increasing at an ever-growing pace. This motivates the research and development of new computation technologies that would provide alternatives to classical silicon-based computers. Based on the theoretical framework developed by Shannon [42], Landauer showed that “Information is physical” [25]. Loosely speaking, this suggests that the abstract notion of information needs to rely on some kind of physical encoding and processing in order to exist. However, there is no physical law imposing that information can only be processed on silicon or biological carbon-based devices. These materials are just two different instances of *computronium*, which is a term coined by Toffoli and Margolus [2] to designate any substrate able to compute. These elements suggest that a shift towards a new computation paradigm is possible.

Optical computers have been investigated for many years. Because they use light as information carrier, their characteristic speed is inherently close to the maximum one allowed in our Universe. In their article [9] Caulfield and Dolev envision them as the natural choice when it comes to finding the computation paradigm of tomorrow because they claim that optical computers can be fast, energy efficient, and generate less heat. They argue that silicon-based devices are reaching their physical limits in terms of bandwidth and heat dissipation, and that great improvements have been realised as far as all optical boolean logic is concerned. Moreover, they point out the fact that optical computers do not necessarily have to mimic the computation logic of classical computers to work, and that future designs should take advantage of physical properties specific to light. The practical study of such a device is the main goal of this work.

In this master thesis, the experimental study of the interferometric stabilisation of a fibre-based optical reservoir computer is tackled. Its first part introduces the concept of reservoir computing, which is a subclass of recurrent neural networks achieving state of the art performances in tasks involving the processing of time dependent data. Reservoir computers differ from classical neural networks by the fact when they are being trained, they only require their output weights to be updated, which makes them computationally attractive. The mathematical model governing the time evolution of a reservoir computer imposes so little conditions that it is possible to reproduce its dynamics using a physical system other than classical computers. The literature shows that this has already been done a couple of times using optical setups, but so far, only a time division multiplexing of the neurons has been implemented, which limits the processing speed.

In the second chapter, a fibre-based photonic reservoir computer relying on wavelength division multiplexing of the neurons is presented. Each of the neurons is encoded in a different wavelength of an electric field evolving inside a fibre loop cavity. The wavelength mixing of the different neurons is performed by a phase modulator. However, because of the physical properties of phase modulators, only a few neurons can be used at the same time. The main advantage of this innovative scheme is a theoretical increase in the processing speed, because multiplexing the neurons in the wavelengths instead of the time allows the input data to reach all the neurons simultaneously.

The third part of the thesis is devoted to the experimental characterisation of the stabilisation performances of the optical cavity used as the reservoir computer. The phase acquired by the electric field each time it goes around the cavity is an important parameter which has an influence on the performances of the reservoir computer and that should be kept under control. The classical cavity stabilisation technique uses the power reflected by the cavity, which is a feature linked to interferometry, to estimate the phase and uses well known control theory methods to regulate it. However, in this experiment, new difficulties arise due to the fact that the light signal used to stabilise the cavity happens to be modulated in intensity because it carries the data to be processed. A possible solution to overcome this issue is to use the Pound-Drever-Hall stabilisation technique which is a powerful tool allowing to stabilise cavities with greater precision. Its main advantage over the classical technique is that, by phase modulating the laser wave and by performing some electronic post-processing, the signal it measures conveys more information about the phase inside the cavity and allows to carry out a better regulation. This stabilisation technique has been implemented on the experiment, and the quality of the stabilisation has been assessed for different Pound-Drever-Hall parameters in order to determine for which ones the cavity is the most likely to be stable enough to operate as a reservoir computer.

The last part of this work comes back to the main results encountered throughout this year of research, and concludes by indicating the factors that should be further investigated in order to refine the characterisation carried out in this thesis.

Chapter 2

Reservoir Computing

Reservoir Computing (RC) is a bio-inspired artificial Recurrent Neural Network (RNN) which is based on the Echo State Network (ESN) introduced by Herbert Jaeger in [19]. This computation scheme is well suited for real-time data processing and for chaotic time series prediction[19, 20, 27], and achieves state of the art performances in those domains, as well as in speech recognition[47, 44, 23], nonlinear channel equalisation[19] and financial forecasting [4].

The first section of this chapter introduces the different concepts linked with RC. It starts by giving a brief overview on the Neural Network (NN) computation paradigm from which RC has been derived. After that, the structure, operating principles and features of Reservoir Computer (RC) are presented. Then, a few elements of Machine Learning (ML) are mentioned in order to have a first glimpse of the training procedure of a RC. The second section is devoted to the mathematical model governing a RC. The last one is about Photonic Reservoir Computers. During the last decade, several physical implementations of RC have been proposed, some of which being optical setups. This kind of RC is presented, and most specifically reservoir involving Time Division Multiplexing (TDM). Finally, a RC is used to resolve two different benchmark tasks and the results of the computations are shown.

2.1 Reservoir Computing framework

2.1.1 Artificial Neural Network

A RC is specific kind of NN, which is a computation paradigm mimicking the behaviour of a biological brain. The artificial neurons are simply interconnected entities carrying an activation level. The way the activation level is updated depends on the scheme, but the basic idea is common for all of them: a neuron receives a linear combination of the activation level of the neurons to which it is connected, and then computes a nonlinear transformation of this value. This gives a new activation level. In figure 2.1, a feedforward NN is depicted. It is called feedforward because the computation goes from left (input neurons in red) to right (output neurons in green). Feedforward NN are organised in layers, and a neuron from one layer can only be influenced by neurons in the adjacent layers. This is shown in the figure by the arrows representing the connections. The gray neurons in the middle belong to the hidden layers, which are used to improve the computational power of such networks. The results of a computation can be read on the activation level of the output neurons [39, p.727][5, p.225].

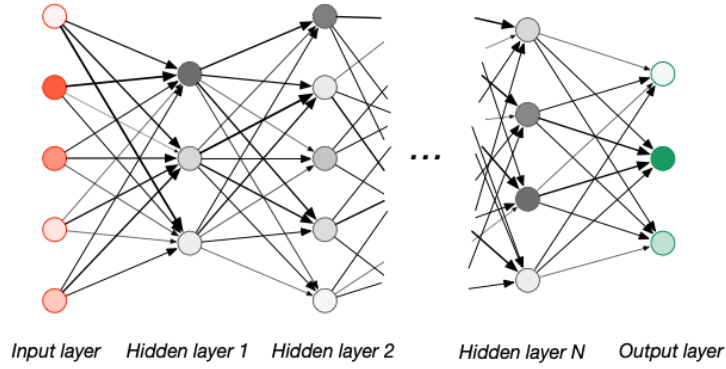


Figure 2.1: Schematic representation of a feedforward NN. The red, gray and green dots represent the input, hidden, and output neurons, respectively. The opacity of the dots schematise the activation level of the neurons, and the width of the arrow connecting two neurons represents how strongly this two neurons are connected.

2.1.2 Reservoir Computing

RC have been designed to process time dependent inputs, so their structure is inherently different from that of a feedforward NN, because they need to exhibit other properties. In this scheme, all the neurons are interconnected and form what is called a reservoir. The reservoir is fed with the time dependent input signal it should process. When the reservoir is properly set up, the activation level of each of the neurons becomes a systematic transformed version of the input signal [19]. This operating point is called the echo state and allows RC to reach their best performances [18, 20]. In this regime, RC exhibit a short-term memory of the previous inputs [19], which could explain why they perform so well in time dependent situations. There are many physical implementations of RC proposed in the literature, many of which are based on optical setups [40], that is why section 2.3 is devoted to them.

In figure 2.2, a RC is shown. The neurons of the reservoir are represented in orange. They characterise what is called the state of the reservoir, which is encoded by $\mathbf{x}(t)$. They are coupled by the connection matrix \mathbf{W} . The input signal $u(t)$ is fed into the input neuron (blue) and is coupled to the reservoir *via* the input matrix \mathbf{W}^{in} . The output $y(t)$ is read on the output neuron (red) and is obtained thanks to the output matrix \mathbf{W}^{out} . This matrix is the only one that needs to be updated when the reservoir is learning. This task is not straightforward, that is why the next paragraph takes care of introducing the different approaches that can be followed to compute \mathbf{W}^{out} . For some applications, it can be useful to also have a feedback of the output sent back into the reservoir. This can be achieved by introducing a feedback matrix \mathbf{W}^{fb} . The mathematical aspects mentioned in this paragraph are detailed in section 2.2.

2.1.3 Machine Learning

Regardless of the learning scheme adopted to train a NN, the basic idea is always to minimise the difference between the desired and the actual outputs. In practice, this is achieved by updating the different connection coefficients of the NN [5, p.233][39, p.733]. This procedure often turns out to be a really complicated task for feedforward NN, which explains why the development of efficient ML algorithms is such a hot research topic nowadays. In contrast, as can be seen in figure 2.3, RC only need their output weights to be adjusted when being trained, which makes them computationally lighter [19]. This is

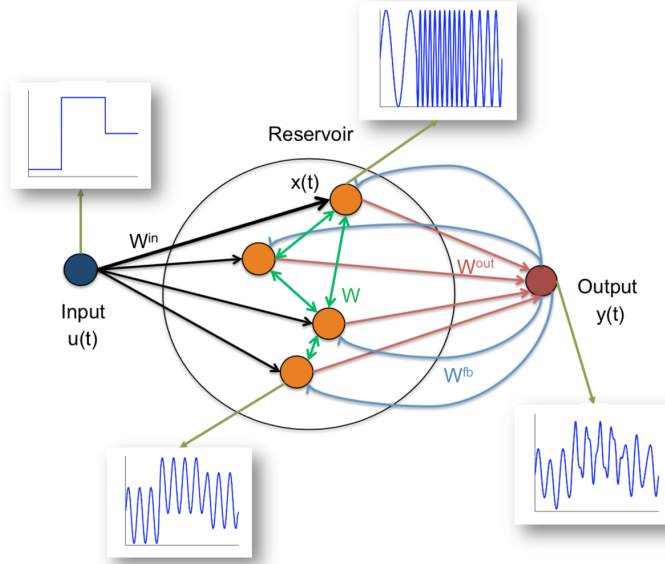


Figure 2.2: Schematic representation of a Reservoir Computer [4]. The orange, blue and red dots represent the reservoir, input and output neurons, respectively. The black arrows labelled \mathbf{W}^{in} , the green ones labelled \mathbf{W} , the red ones labelled \mathbf{W}^{out} and the blue ones labelled \mathbf{W}^{fb} represent the input weights, the connection weights, the output weights and the feedback weights, respectively.

due to the fact that the connections of the reservoir should not contain any information about the task, but should only be used to reach the ESN regime, as mentioned in the previous paragraph. There are two main families of training methods for RC [21]. On the one hand, there is the *batch learning*, which comprises the methods requiring to first store a wealth of data regarding the task being taught before being able to actually compute the output weights. Once enough data is gathered, this kind of algorithms returns the optimal weights all at once. They present the advantage of involving only one training phase, after which the RCs are ready to perform. However, the need for vast amount of data and the inability for the RC to adapt to an input evolving out of the range for which it has been trained are two drawbacks. On the other hand, *online learning* methods allow to iteratively improve the output weights. Therefore, starting from a first guess, these algorithms can converge to suitable output weights. They are much more adaptable than the batch learning ones. However, their convergence is not guaranteed and can be slow [22, 41].

2.2 Mathematical Model

In this section, an overview of the mathematical framework is given. First, the different objects are formally defined, and their dynamics is presented. Then, a few key elements about the computation of the output weights are introduced.

2.2.1 Dynamics of the reservoir

As said previously, the RC can be fully described by the activation level of each of its neurons. The state of the RC can therefore be defined as a vector whose components are the activation levels of the neurons. If the number of neurons making up the reservoir is N , and if x_i is the activation level of the i^{th} neuron, then the state vector reads as follows:

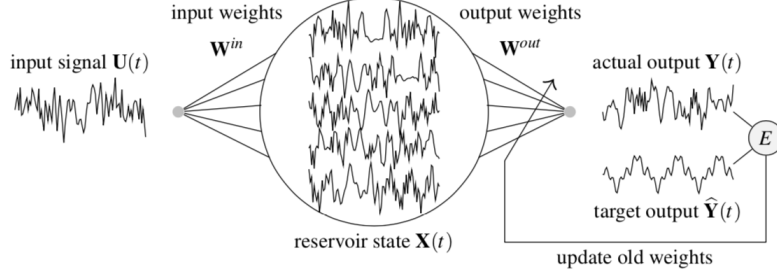


Figure 2.3: Learning procedure for Reservoir Computer [18]. The input signal $\mathbf{u}(t)$ is sent into the reservoir using the input weights \mathbf{W}^{in} and disturbs the reservoir state $\mathbf{X}(t)$. The activation level of the neurons are combined using the output weights to compute the output $\mathbf{Y}(t)$, which is compared to the desired output $\hat{\mathbf{Y}}(t)$ to produce the error. The error is processed by aML algorithm in order to update the output weights \mathbf{W}^{out} .

$$\mathbf{x} = \begin{bmatrix} x_1 \\ \vdots \\ x_i \\ \vdots \\ x_N \end{bmatrix} \quad (2.1)$$

The dynamics governing the state vector and the output of the reservoir proposed in [20] are presented below. In practice, it is too general for the implementations studied in this work. However, the equations are introduced without loss of generality, and simplifying assumptions applying the photonic implementations of RC will be specified in the section devoted to them.

$$\mathbf{x}(n+1) = \mathbf{f}(\mathbf{W}^{\text{in}}\mathbf{u}(n+1) + \mathbf{W}\mathbf{x}(n) + \mathbf{W}^{\text{fb}}\mathbf{y}(n)) \quad (2.2)$$

$$\mathbf{y}(n+1) = \mathbf{f}^{\text{out}}(\mathbf{W}^{\text{out}}(\mathbf{x}(n+1), \mathbf{u}(n+1), \mathbf{y}(n))) \quad (2.3)$$

Different elements need to be defined:

- $n \in \{1, \dots, T\}$ is the discrete time variable
- $\mathbf{u} \in \mathbb{C}^k$ is the input vector which enters the reservoir through the input neurons
- $\mathbf{W}^{\text{in}} \in \mathbb{C}^{N \times k}$ is the input matrix. It indicates how the k input neurons are connected to the neurons of the reservoir
- $\mathbf{x} \in \mathbb{C}^N$ is the state vector, as said previously
- $\mathbf{W} \in \mathbb{C}^{N \times N}$ is the synaptic matrix, or the connection matrix which has already been introduced
- $\mathbf{y} \in \mathbb{C}^m$ is the output vector of the reservoir whose value can be read out on the output neurons
- $\mathbf{W}^{\text{fb}} \in \mathbb{C}^{N \times m}$ is the feedback matrix. It couples the output back into the reservoir
- $\mathbf{f} : \mathbb{C}^N \mapsto \mathbb{C}^N$ is the nonlinear function mapping the linear combination it receives as argument to a valid state vector

- $(\mathbf{x}(n+1), \mathbf{u}(n+1), \mathbf{y}(n))$ is the concatenation of those three vectors
- $\mathbf{W}^{\text{out}} \in \mathbb{C}^{m \times (N+k+m)}$ is the output matrix of the reservoir. It is optimised through ML
- $\mathbf{f}^{\text{out}} : \mathbb{C}^m \mapsto \mathbb{C}^m$ is the output function of the reservoir

2.2.2 Computation of the output weights

To determine the output matrix \mathbf{W}^{out} in the batch learning approach, one needs to perform a ridge (or Tikhonov) regression [44], which is an improved version of multivariate linear regression that improves the numerical stability of the scheme, and that prevents overfitting of the data. By restricting the desired output to a scalar function $\hat{y}(n)$ and by taking a learning period of T time steps, one defines the matrices \mathbf{X} and $\hat{\mathbf{Y}}$ and solves the following equation to find the output weights vector \mathbf{W}^{out} :

$$\mathbf{X} = \begin{bmatrix} x_0(0) & x_1(0) & \dots & x_N(0) \\ x_0(1) & x_1(1) & \dots & x_N(1) \\ \vdots & & & \vdots \\ x_0(T) & x_1(T) & \dots & x_N(T) \end{bmatrix}, \quad \hat{\mathbf{Y}} = \begin{bmatrix} \hat{y}(0) \\ \hat{y}(1) \\ \vdots \\ \hat{y}(T) \end{bmatrix} \quad (2.4)$$

$$(\mathbf{X}^T \mathbf{X} + \varepsilon \mathbf{I}) \mathbf{W}^{\text{out}} = \mathbf{X}^T \hat{\mathbf{Y}} \quad (2.5)$$

Here ε is the constant used for the Tikhonov regression. By setting ε to 0, one finds the *normal equation* that comes up when solving a linear regression [18] in the sense of the least squares. This procedure can be generalised to higher dimensions desired output vectors $\hat{\mathbf{y}}(n)$. Different optimisation algorithms can be used to compute the output weights in practice, but their description is out of the scope of this work, see [26] for more details.

Different metrics can be used to capture the distance between the actual and the desired outputs. In the literature, one of the most frequent ones is the Normalised Mean Square Error (NMSE) [15], with $\hat{\mathbf{y}}(n)$ the target vector, $\langle \dots \rangle_n$ the average with respect to n , and $\| \dots \|$ the euclidean norm:

$$\text{NMSE} = \frac{\langle \|\hat{\mathbf{y}}(n) - \mathbf{y}(n)\|^2 \rangle_n}{\langle \|\hat{\mathbf{y}}(n) - \langle \hat{\mathbf{y}}(n) \rangle_n\|^2 \rangle_n} \quad (2.6)$$

2.3 Introduction to Photonic Reservoir Computing

As already mentioned, different implementations of Photonic Reservoir Computing (PRC) have been proposed [40]. In this section, systems in which neurons are multiplexed in time are studied because they constitute a good first approach to PRC and because they bring insights that are interesting for the scheme explored in this thesis. However, it is worth mentioning that one can find among other schemes spatially distributed RC based on fully integrated silicon-chip with nonlinearities stemming from Semiconductor Optical Amplifiers [45], and on diffractively coupled Vertical-Cavity Surface-Emitting Lasers [8].

In this section, the assumptions applying to reservoir with TDM of the neurons are first presented. Indeed, the equations introduced in the previous section can be substantially simplified when one is working with this kind of reservoir. After that, setups where

neurons are encoded in the intensity of the light are considered. Finally, experiments in which the neurons are represented in the phaser of the electric field are presented. Recalling that the energy flux carried by the light is proportional to the squared modulus of the phaser of the electric field:

$$I = \frac{1}{2}cn\varepsilon_0|E|^2 \quad (2.7)$$

with I the energy flux in W m^{-2} , c the celerity of the light, n the refractive index of the medium and E the complex phaser representation of the electric field. It is shown that the outputs of these two kinds of reservoir are different, but analogous, and that they rely on the same mathematical interpretation. The latter scheme is studied with greater length since it reaches state of the art performances in classical benchmark tasks and since the novel implementation which is the main topic of this work shares some features with it. As a last remark, and to give a better understanding on the flexibility of RC, in [16] the researchers managed to perform speech recognition and to resolve the XOR problem¹ in a bucket of water.

2.3.1 Time Division Multiplexing of the neurons

Many implementations of RC based on TDM of the neurons have been proposed in the literature [33, 3, 15, 12, 46, 48]. Let T be the time scale of the input signal. It should be close to the Round Trip Time (RTT) of the delay line, but not exactly the same in order to be able to couple the neurons. The detuning between the RTT and T is controlled by the integer parameter k . In figure 2.4, one can observe how the neurons can be multiplexed in time. One can see that the allocated window for each of the neurons lasts $\theta = T/N$. Since θ cannot be arbitrarily small in practice², this implies that the greater the number of neurons, the greater T and thus the slower the time scale of the input data. This suggests that one should look for a tradeoff between accuracy and speed in data processing for this kind of RC. For example, in [48], the refresh rate of the input is around 0.9 GHz.

2.3.2 Simplifying assumptions

In this section, the mathematical framework introduced in section 2.2 is adapted to describe the behaviour of TDM PRC in a suitable way. Further details concerning specific types of PRC are added in the following sections.

Input and connection matrices The input of the reservoir is a real scalar function $u(n)$ for PRC, therefore the expression of \mathbf{W}^{in} becomes a real vector of length N which is called the *input mask* \mathbf{m} in the literature. The input mask can be chosen in different ways: in [15], they use a sinusoidal input mask whereas in [3, 48, 33] the input masks are randomly chosen.

Very few constraints apply to the creation of the connection matrix \mathbf{W} . It can be randomly generated and sparse. However, to make the occurrence of the echo state more

¹The XOR task consists in reproducing the behaviour of a logical XOR gate, which is a task of historical importance for NN [29].

²If θ gets too short, it exceeds the bandwidth of measurement devices, so it becomes impossible to measure the neurons.

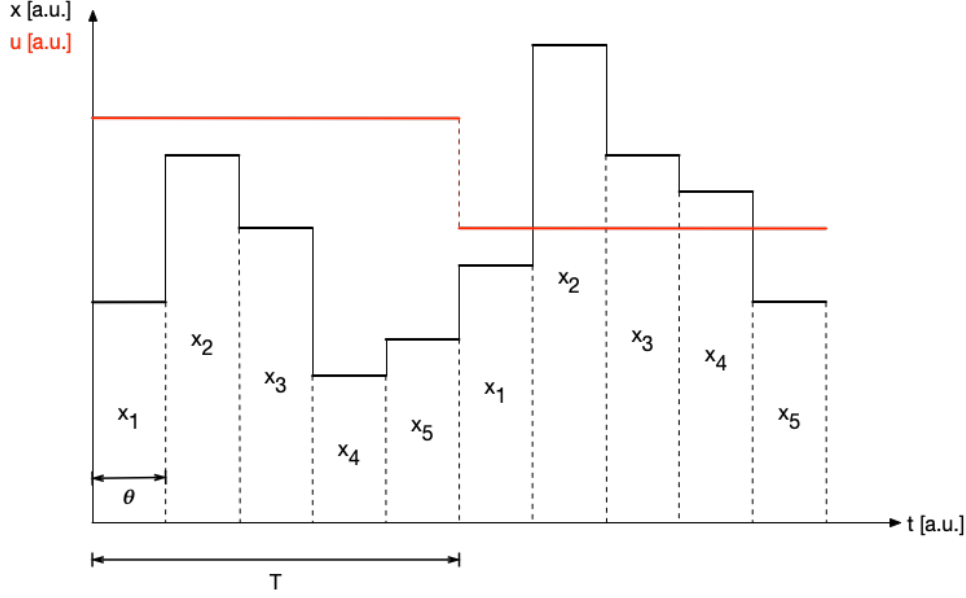


Figure 2.4: Schematic representation of the evolution of the neurons in time for a TDM reservoir. The red signal represents the input data $u(n)$ and the black one represents the evolution of the activation level of the neurons as a function of the time. x_i denotes the slot allocated to the activation level of the i^{th} neuron. T is the duration over which the input is constant and θ is the duration of a slot, $\theta = \frac{T}{N}$.

likely to happen, one wants to work with a spectral radius $\rho(\mathbf{W}) < 1$. If this condition is not verified, as well as degrading the performance of the reservoir, this can also lead to instabilities [26].

The matrices \mathbf{W} and \mathbf{W}^{in} can be rescaled, and this scaling can alter the performances of the reservoir. One should therefore design the PRC in such a way that those scaling factors are easily accessible experimentally. If one defines α and β , the feedback³ and input gains, the input and connection matrices become:

$$\mathbf{W} \longrightarrow \alpha \mathbf{A}, \quad \mathbf{W}^{\text{in}} \longrightarrow \beta \mathbf{m} \quad (2.8)$$

Feedback and output The output signal of a PRC is a real scalar function $y(n)$, which means that the output matrix \mathbf{W}^{out} becomes a real vector. Furthermore, the concatenation of $\mathbf{x}(n+1), \mathbf{u}(n+1), y(n)$ appearing in equation (2.3) is not used, only the state vector \mathbf{x} is used, hence the fact that \mathbf{W}^{out} is of dimension N . Regarding the feedback of the output into the reservoir, it is not implemented in practical RC experiments.

With all these simplifications, equations (2.2) and (2.3) reduce to:

$$\mathbf{x}(n+1) = \mathbf{f}(\alpha \mathbf{A} \mathbf{x}(n) + \beta \mathbf{m} u(n+1)) \quad (2.9)$$

$$y(n+1) = f^{\text{out}}(\mathbf{W}^{\text{out}} \mathbf{x}(n+1)) \quad (2.10)$$

³This may seem like a misnomer at this point since it has nothing to do with \mathbf{W}^{fb} , but this name is used because α acts as a gain for the activation level of the neurons being fed back into the reservoir.

2.3.3 Neurons encoded in light intensity

There are two major families of TDM PRC. The first kind of PRC are those using optical components exhibiting nonlinear behaviour, such as Mach-Zehnder Modulator (MZM) [15, 33, 3], Semiconductor Optical Amplifier (SOA) [46] or semiconductor saturable absorber mirror [12]. In an actual optical experiment, the measurements have to be done with photodiodes. These devices can only inform about the intensity of the light, which is proportional to the squared modulus of the phaser representation of the electric field, and not about the actual electric field. However, in the scheme presented above, the input and the activation level of the neurons are real valued functions appropriately encoded in the intensity of the light, and can therefore be directly read out by a photodiode, hence this simple expression for the output of the reservoir:

$$y(n+1) = \sum_{i=1}^N W_i^{\text{out}} x_i(n+1) = (\mathbf{W}^{\text{out}})^T \cdot \mathbf{x}(n+1) \quad (2.11)$$

2.3.4 Neurons encoded in phaser representation of the electric field

On the other hand, in [48], the neurons are encoded in the complex phaser representation of a coherent electric field and are linearly coupled using a delay line. In this scheme, the reservoir is linear, as can be seen on equation (2.13). This kind of RC is described with greater length because the new approach studied in this thesis relies on a linear reservoir as well. In this equation, α and β are the feedback and input gains, respectively, A_0 is the input bias, ϕ is the phase acquired by the electric field after one trip around the delay line, and k is the detuning parameter.

$$x_i(n+1) = \begin{cases} \alpha e^{j\phi} x_{i-k}(n) + \beta (m_i u(n) + A_0) & \text{if } k \leq i \leq N \\ \alpha e^{j\phi} x_{N+i-k}(n-1) + \beta (m_i u(n) + A_0) & \text{if } 0 \leq i \leq k \end{cases} \quad (2.12)$$

The equation can be rewritten in a compact way:

$$\mathbf{x}(n+1) = \alpha \mathbf{A} \mathbf{x}(n) + \beta (\mathbf{m} u(n+1) + \mathbf{A}_0) \quad (2.13)$$

It thus appears more clearly why the condition mentioned previously regarding $\rho(\alpha \mathbf{A})$ is relevant. Indeed, by neglecting the inputs, if \mathbf{x}_j is an eigenvector of $\alpha \mathbf{A}$ with eigenvalue $\lambda_j > 1$, the above equation will lead to an exponential divergence $\mathbf{x}_j(n) \sim \lambda_j^n \mathbf{x}_j(0)$. On the other hand, if λ_j is too small, the state \mathbf{x}_j will be damped too quickly, deteriorating the short-term memory capabilities of the reservoir and preventing it from reaching the echo state.

In the linear reservoir, since the neurons and the input are inscribed in the complex electric field, the nonlinearity is introduced by the read out photodiodes. The output is therefore given by:

$$y(n+1) = \sum_{i=1}^N W_i^{\text{out}} |x_i(n+1)|^2 \quad (2.14)$$

From a historical point of view, it is interesting to notice that this reservoir shares features with the first artificial NN, the *perceptron*, introduced by F. Rosenblatt in 1958 [38], which also had a linear connection matrix, and a nonlinear output function.

Equations (2.11) and (2.14) give an interesting intuition on the meaning of the ESN. Indeed, as said previously, when a RC reaches the echo state, each of the neurons exhibits a tendency to systematically reproduce a modified version of the input, the modification being an individual characteristic of each neuron [19]. One can see this feature in the perspective of linear algebra. When the RC is fed with an input, it creates a set of time varying functions that can be seen as a basis in which one can try to express the output of the reservoir, which is a vector in the vectorial space of functions. This is why it is often said in the literature that a RC maps an input to a higher dimensional space. Therefore, one can in theory approach any target function with an arbitrary precision, depending on the number of neurons in the reservoir [19]. The higher the number of neurons, the closer to a genuine series development one gets.

2.3.5 Simulations

In this section, the performance of the linear reservoir with quadratic output from [48] are estimated with simulations. Two benchmark task are tackled, first NARMA10 and then nonlinear channel equalisation.

NARMA10

Nonlinear Auto-Regressive Moving Average (NARMA) 10 is a model often used to simulate chaotic time series because it exhibits similar properties [33]. If $u(n)$ is a random variable uniformly distributed along the interval $[-0.5, 0.5]$, the recurrent equation for NARMA10 reads:

$$\hat{y}(n+1) = 0.3\hat{y}(n) + 0.05\hat{y}(n) \left(\sum_{i=0}^9 \hat{y}(n-i) \right) + 1.5u(n-9)u(n) + 0.1 \quad (2.15)$$

Nonlinear channel equalisation

This task consists in the reconstruction of a signal after it has travelled through a non-linear channel. The emitted signal \hat{y} is randomly drawn from the symbol set $\{-3, -1, 1, 3\}$. It is first superimposed with following and preceding symbols as can be seen in (2.16). After that, a third degree polynomial transformation is applied to the mixed signals, and a Gaussian noise, whose intensity can be set in order to adjust the Signal to Noise Ratio (SNR), is added in (2.17). The metric used to evaluate the performance of the reservoir for this type of task is the Signal Error Rate (SER) and is defined as the ratio between the number of erroneous symbols and the total number of symbols.

$$\begin{aligned} q(n) = & 0.08\hat{y}(n+2) - 0.12\hat{y}(n+1) + \hat{y}(n) + 0.18\hat{y}(n-1) \\ & - 0.1\hat{y}(n-2) + 0.091\hat{y}(n-3) - 0.05\hat{y}(n-4) \\ & + 0.04\hat{y}(n-5) + 0.03\hat{y}(n-6) + 0.01\hat{y}(n-7) \end{aligned} \quad (2.16)$$

$$u(n) = q(n) + 0.036q(n)^2 - 0.011q(n)^3 + \nu(n) \quad (2.17)$$

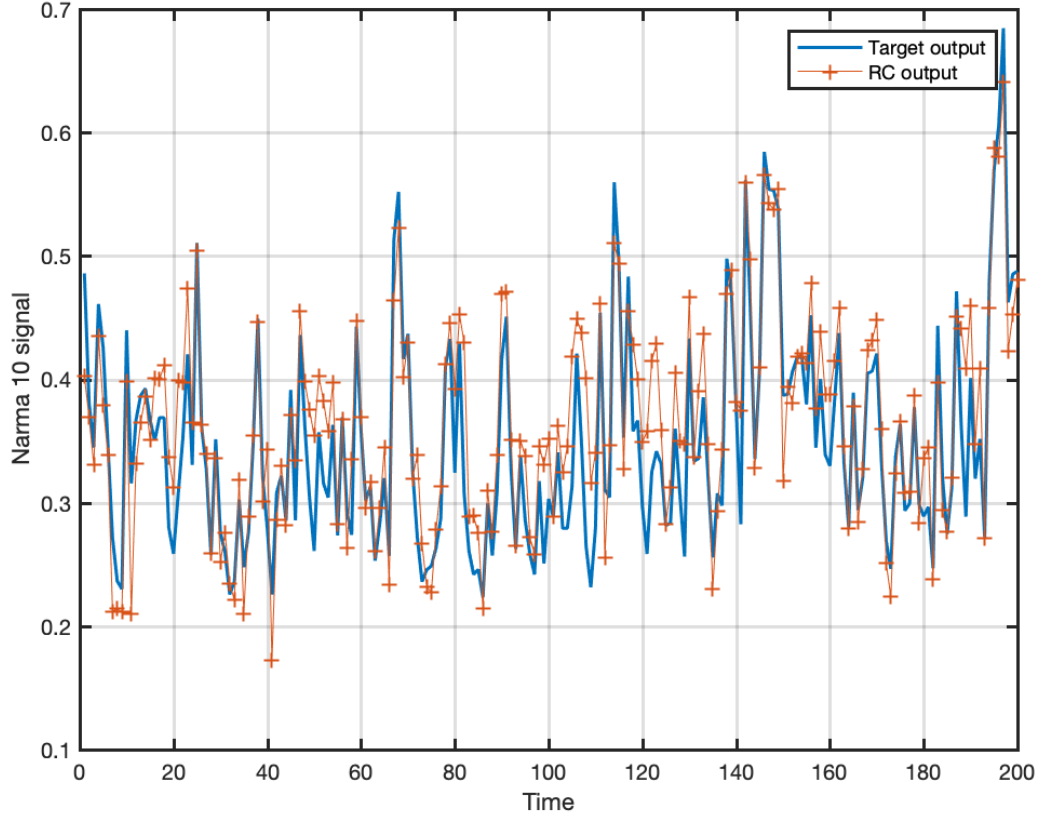


Figure 2.5: NARMA10 task with NMSE equal to 0.1541. This reservoir is made of 50 neurons. $\alpha = 0.5$, $k = 7$, $\phi = 0$ rad, $\beta = 1$, $A_0 = 1$, \mathbf{m} is a random vector distributed between 0 and 1. The first 300 time steps were discarded in order to let enough time to the reservoir to enter the echo state (washout). Then the reservoir was trained for 3000 time steps and tested over 6000 time steps. This reservoir is particularly well suited for NARMA10 since the nonlinearities in the signal are mostly quadratic.

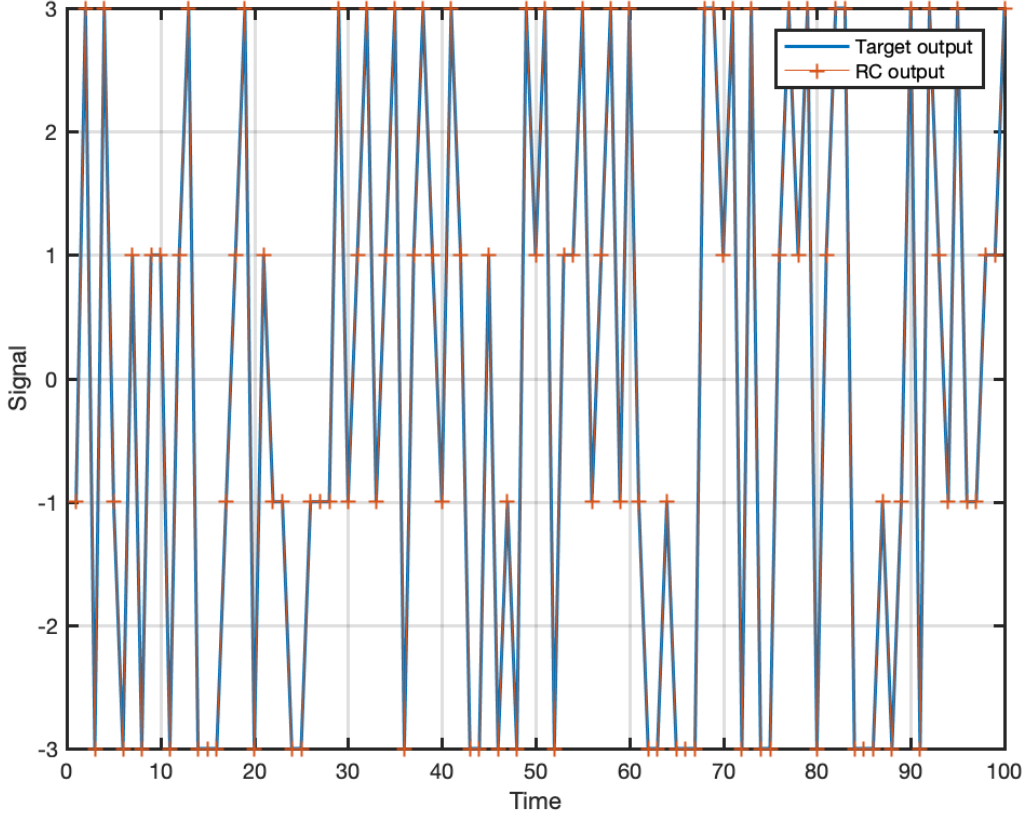


Figure 2.6: Nonlinear channel equalisation task with a signal error rate of $5 \cdot 10^{-4}$, with SNR equal to 32 dB. This reservoir is made of 50 neurons. $\alpha = 0.5$, $k = 7$, $\phi = 0$ rad, $\beta = 1$, $A_0 = 1$, \mathbf{m} is a random vector distributed between 0 and 1. The first 300 time steps were discarded in order to let enough time to the reservoir to enter the echo state (washout). Then the reservoir was trained for 3000 time steps and tested over 6000 time steps. The symbols predicted by the RC are found by rounding the continuous valued output to the closest symbol.

Chapter 3

Photonic Reservoir Computer with Wavelength Division Multiplexed neurons

In this chapter, a novel approach of PRC is proposed, in which the neurons are no longer multiplexed in time, but in wavelength (or frequency) instead. This scheme was introduced in [1] and its end goal is to overcome the speed limitations imposed by the TDM of the neurons, as exposed in section 2.4. Indeed, by multiplexing the neurons in the frequency domain, the input signal can reach them all at the same time, there is no need to slow down its pace to let it alter the neurons sequentially. As an illustration, in [45], they proposed the first PRC with parallelisation of the neurons. In the experiment described in the paper, the neurons were spatially multiplexed. Doing so, the authors were able to reach data processing rates up to 12.5 GHz on tasks such as header recognition or boolean logic, which is an increase of one order of magnitude compared to those reported in [48]. This is encouraging for research in parallel PRC and motivates the study of the scheme explored in this thesis.

First, in section 3.1, a description of the working principle is given. It starts with a high-level overview of the scheme in which different features and components are presented. After that, attention is brought to the frequency coupling mechanism used to let the neurons interact between one another. It is shown that this can be achieved using a optoelectronic Phase Modulator (PM), even though this device has some practical drawbacks.

3.1 Description of the scheme

In this section, the working principle of Wavelength Division Multiplexing (WDM) PRC is first given. This scheme takes advantage of the wave character of light and uses different wavelength to encode the neurons. It is fibre-based and relies on an optical cavity made of a fibre loop. Inside the cavity, the different neurons need to be able to interact, therefore one has to provide some coupling mechanism for the different frequencies. This issue is tackled in section 3.1.2 and provides interesting mathematical insights that are eventually used to derive a suitable model for this kind of linear RC.

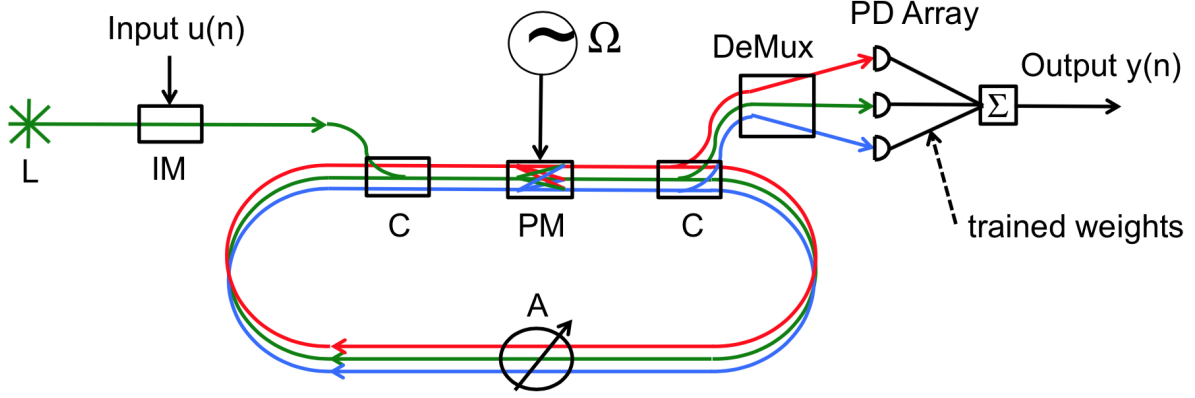


Figure 3.1: Schematic representation of the working principle of the WDM PRC [1]. A monochromatic laser sends light which is modulated in intensity to carry the data $u(n)$. It is coupled into a ring cavity through the coupler on the left side. It undergoes phase modulation and amplification during one round trip in the cavity. It exits the cavity by the coupler on the right side and is demultiplexed. The signals read by the photodiodes in the array are linearly combined using the output weights to construct the output of the reservoir.

3.1.1 Working principle

The working principle of the new reservoir is schematised in figure 3.1. The whole setup is fibre-based, and the fibre used is a polarisation maintaining, single mode fibre.

Input The input time series $u(n)$ is converted into a continuous signal $\tilde{u}(t)$ by keeping its value constant during one period τ (sample and hold procedure), which leads to $\tilde{u}(t) = u(n)$, with $t \in [n\tau, (n+1)\tau[$. The continuous, coherent light emitted by a narrow band laser at frequency ω is modulated in intensity by the input signal $\tilde{u}(t)$ using a MZM.

Cavity The modulated data is then coupled to a ring cavity around 20 metres long¹. Inside this cavity, a PM mixes the different optical frequencies. More information about the PM can be found in section 3.1.2. Losses are introduced inside the cavity by two main sources, the intrinsic losses of the fibre and the insertion losses of the PM, hence the presence of an intra-cavity amplifier used to compensate for them. The neurons are encoded in the electric field evolving inside this cavity, which is schematised on the figure by the three different colours for the fibre loops. Therefore, from now on, the cavity can be referred to as the *reservoir*. The holding time τ introduced earlier should be equal to the RTT of the reservoir. This is done in order to update the discrete dynamics of the RC each time the light completes a trip around the cavity. Doing so, one ensures that the value of the neuron x_j at discrete time $n+1$ depends on the values of the neurons x_i , with $i \in \{1, \dots, N\}$, at precisely time n .

Readout The electric field encoding the neurons exits the cavity through another coupler, and is then demultiplexed in frequency. Each of the frequency component is measured using a Photodiode (PD), which gives a value proportional to the squared modulus

¹The length of the cavity can be derived from its Free Spectral Range (FSR), which is studied in the next chapter.

of the electric field, as explained in the previous chapter. The resulting signals are linearly combined using the trained output weights to produce the output of the reservoir $y(n)$.

$$y(n) = \sum_{i=1}^N W_i^{\text{out}} |x_i(n)|^2 \quad (3.1)$$

Training and testing The training scheme used for this setup is the batch learning. Thus, to compute the output weights \mathbf{W}^{out} , one can use the ridge regression technique introduced in section 2.2.2. To do so, one needs to discard the first state vectors \mathbf{x} because they correspond to the transient of the reservoir, and then to store them² as well as the desired outputs \hat{y} during the whole learning period to create the matrices \mathbf{X} and $\hat{\mathbf{Y}}$. After that, it is straightforward to solve equation (2.5) and to find the output weights. Once the RC is trained, it can move on to the testing phase, during which the outputs $y(n)$ are compared to the desired outputs. From that, one can quantify the performance of the RC using the appropriate metric, such as the NMSE or the SER for example.

3.1.2 Frequency coupling of the neurons

To mix the different frequencies present inside the reservoir a PM is used. This kind of device is well known for creating equidistant frequency sidebands. Let $Ee^{i\omega t}$ be the input electric field entering the PM. Since a PM is an optoelectronic device, it needs to be externally driven by a voltage generator with a RF modulation signal $V_{\text{RF}}(t) = m \sin(\Omega t)$, with $\Omega \ll \omega$. Using the *Anger-Jacobi* expansion that allows to express the exponential of a trigonometric function in the basis of its harmonics, one can express the effect of a PM:

$$\begin{aligned} Ee^{i\omega t} &\xrightarrow{\Omega} Ee^{i\omega t} e^{im \sin(\Omega t)} \\ &= E \sum_{n=-\infty}^{\infty} J_n(m) e^{i(\omega+n\Omega)t} \end{aligned} \quad (3.2)$$

This formula indicates that the resulting wave is a discrete superposition of planar waves whose frequencies are evenly spaced ($\Omega/2\pi$ between each frequency component) and centred on the input electric field frequency $\omega/2\pi$. The coefficient $J_n(m)$ weighting the superposition is the n^{th} order Bessel function and m is the modulation depth.

However, what can already be said about m is that without external amplification, it cannot exceed 2 in practice. This is due to the fact that when one increases the modulation frequency $\Omega/2\pi$, the modulation amplitude A cannot be brought to arbitrarily large values. As a crude approximation regarding the RF generator, one could say that the product ΩA is upper bounded. In figure 3.2, one can observe the behaviour the Bessel functions $J_n(m)$ with $n \in \{0, \dots, 6\}$. For $m \in [0, 2]$, $J_n(m)$ becomes less significant for increasing order n . This provides an insight on an intrinsic limitation of this kind of RC, which is the limited number of neurons. A possible solution to improve the scheme would be to use a longitudinal multimode laser³ to inject energy in a wider range of neurons. Yet, the coupling between distant neurons would still be very faint.

²Since the output y is constructed using the squared modulus of the activation of the neurons, the matrix \mathbf{X} is filled with $|x_i(n)|^2$ instead of $x_i(n)$ as suggested in section 2.2.2.

³A longitudinal multimode laser emits light at different frequencies.

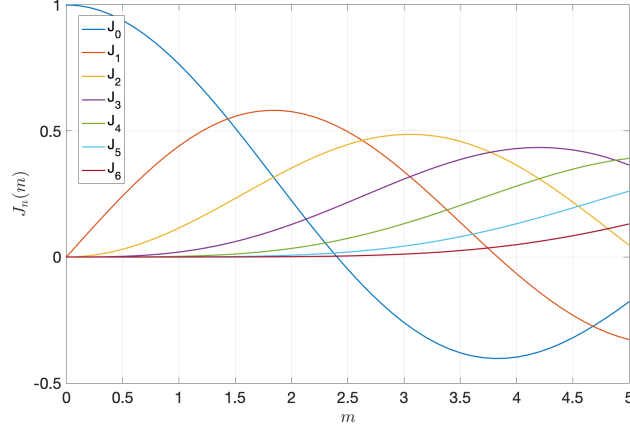


Figure 3.2: Bessel function of order $n \in \{0, \dots, 6\}$.

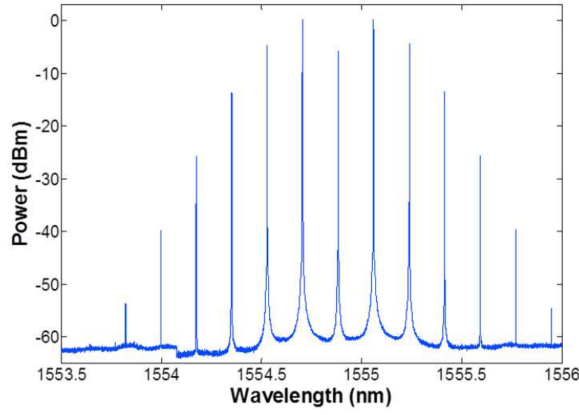


Figure 3.3: Experimental spectral density inside the reservoir [1]. This is the spectrum measured after passing through the PM for an incident monochromatic wave with a wavelength of $1.555 \mu\text{m}$.

In figure 3.3, the elements regarding the fast decrease of the intensity of the sidebands brought to light in the previous paragraph are confirmed experimentally. On this graph, one can see that only 13 neurons are usable in practice. One also notices that the spectrum is symmetric with respect to the central neuron. This can be explained by the fact that the height of the n^{th} peak is $\propto |J_n(m)|^2$, and by using a property of the Bessel functions that says that for $n \in \mathbb{Z}$, $J_{-n}(m) = (-1)^n J_n(m)$:

$$|J_{-n}(m)|^2 = |(-1)^n J_n(m)|^2 = |J_n(m)|^2 \quad (3.3)$$

3.1.3 Mathematical model

This section tackles the derivation of the discrete equation governing the dynamics of the reservoir. This calculation relies on the result stemming from the previous section regarding the effect of a PM on an incident electric field. As a first step, the state \mathbf{x} is expressed using a convenient formalism. The end goal is to reformulate the problem in terms of vectors, to harness linear algebra. Let N be the total number of neurons. This implies that \mathbf{x} should be a N -dimensional vector that can be developed as a linear combination of basis vectors:

$$\mathbf{x} = \sum_{i=1}^N x_i \hat{\mathbf{e}}_i \quad (3.4)$$

If the basis vectors are adequately chosen, the state vector \mathbf{x} can reduce to the value of the electric field inside the reservoir. The basis vectors are defined as:

$$\hat{\mathbf{e}}_n = e^{i\omega_n t} = e^{i(\omega + n\Omega)t} \quad (3.5)$$

Moreover, to be consistent, the numbering of the neurons should be modified such that $\hat{\mathbf{e}}_0$ corresponds to the central frequency. Let η be the new variable used to iterate through the neurons such that the sum in the linear combination will go from $-\eta$ to η instead of from 1 to N . η is given by $\lfloor N/2 \rfloor$. The state vector \mathbf{x} now reads:

$$\mathbf{x} = \sum_{i=-\eta}^{\eta} x_i \hat{\mathbf{e}}_i \quad (3.6)$$

This is rigorously equal to the electric field inside the reservoir. The results from the previous section can now be used to derive the discrete dynamics equation. Knowing the value of each of the neurons at discrete time n and the effect of a PM, one can compute the new state vector. To do so, linear algebra is used. One knows that the reservoir is linear, therefore, it should be possible to find a linear mapping between two successive states. If there exists a linear mapping, since one is working in discrete space, there is a matrix representation of this mapping. Furthermore, given that one knows the effect of a PM on each of the basis vectors, one can explicitly define this matrix.

$$\mathbf{J} = \begin{bmatrix} J_0(m) & J_{-1}(m) & \dots & J_{-\eta}(m) & \dots & J_{-2\eta}(m) \\ J_1(m) & J_0(m) & \dots & J_{-\eta+1}(m) & \dots & J_{-2\eta+1}(m) \\ \vdots & \vdots & & \vdots & & \vdots \\ J_{2\eta}(m) & J_{2\eta-1}(m) & \dots & J_{\eta}(m) & \dots & J_0(m) \end{bmatrix} \quad (3.7)$$

One should note that each time the light goes around the cavity, it acquires some phase which is dependent on the wavelength. This should be taken into account in the derivation as well. If ϕ_i is the phase acquired by the neuron propagating with the frequency $\omega_i/2\pi$, one can define the phase matrix:

$$\Phi = \begin{bmatrix} e^{i\phi_{-\eta}} & 0 & \dots & \dots & \dots & 0 \\ 0 & e^{i\phi_{-\eta+1}} & 0 & \dots & \dots & 0 \\ \vdots & 0 & \ddots & & & \vdots \\ \vdots & \vdots & & e^{i\phi_i} & & \vdots \\ \vdots & \vdots & & & \ddots & 0 \\ 0 & 0 & \dots & \dots & 0 & e^{i\phi_{\eta}} \end{bmatrix} \quad (3.8)$$

Both \mathbf{J} and Φ are $N \times N$ matrices, with associated linear operators $\hat{\mathbf{J}}$ and $\hat{\Phi}$. Finally, recalling that α and β are the feedback and input gains, respectively, and that the laser source only injects light in the central wavelength, one can express the discrete time dynamics of the reservoir:

$$\mathbf{x}(n+1) = \alpha \hat{\Phi} \hat{\mathbf{J}} \left(\mathbf{x}(n) + \beta u(n+1) \hat{\mathbf{e}}_0 \right) \quad (3.9)$$

The value of α can be adjusted experimentally by changing the intra-cavity amplification and that of β numerically in the computer controlling the experiment. The output

of the reservoir is obtained by computing a linear combination of the squared modulus of the different neurons, like in equation (2.11):

$$y(n+1) = \sum_{i=-\eta}^{\eta} W_i^{\text{out}} |x_i(n+1)|^2 \quad (3.10)$$

Chapter 4

Interferometric stabilisation of reservoir cavity

4.1 Introduction

In this introductory section, the concept of interferometry is presented. As the name of the chapter suggests, this technique is used to stabilise the reservoir cavity. The reason why an optical cavity needs stabilisation will appear clearer later, but basically, this is due to the fact that light is a wave and that it can interfere with itself inside the cavity. Moreover, it will be shown that the interferometric properties are wavelength dependent. Since several wavelengths coexist inside the reservoir, this gives a first glimpse on the complexity entailing its stabilisation. To gain some insight on interferometry, and before moving on to the study of an actual ring cavity, the features of the well known Fabry-Perot (FP) interferometer are recalled. After that, it is shown that the properties studied for the FP can be translated to ring cavities with close to no modification. Finally, under the light of the basic notions of interferometry developed, the difficulties linked to the stabilisation of the reservoir cavity, which is at the heart of the scheme introduced in this thesis, are presented.

4.1.1 Fabry-Perot interferometer

The FP plays an important role in modern optics as it is really ubiquitous. This can be explained by the fact that, despite its great simplicity, it can reach good performance using high reflectivity mirrors, which can be produced using recent technologies. In practice, a FP cavity is simply made of two mirrors facing each other as can be viewed in figure 4.1. One can see the two mirrors, represented by the vertical black lines, and the different electric fields. The resonance condition, namely the situation where the transmitted electric field E_t is maximum, can be seen intuitively as a situation where the intra-cavity field E_1 is in phase with the incident field E_{in} , which leads to the build up of an intra-cavity standing wave. On the other hand, the anti-resonance condition is met when E_{in} and E_1 are out of phase. The transmissivity of the FP interferometer, which is defined as the ratio $|E_t|^2/|E_{in}|^2$, is given by [34]:

$$\mathcal{T}(\omega) = \frac{1}{1 + \mathcal{F} \sin^2\left(\frac{\omega}{\text{FSR}}\right)} \quad (4.1)$$

In this expression, \mathcal{F} is the finesse of the cavity, ω is the angular frequency of the incident electric field, and FSR is the Free Spectral Range of the cavity. In a stationary regime, the energy inside the cavity does not evolve, therefore the energy carried by the

incident electric field E_{in} can either be transmitted or reflected, which implies that the reflectivity of the cavity which is defined as the ratio $|E_{\text{ref}}|^2/|E_{\text{in}}|^2$ is simply given by:

$$\mathcal{R}(\omega) = 1 - \mathcal{T}(\omega) \quad (4.2)$$

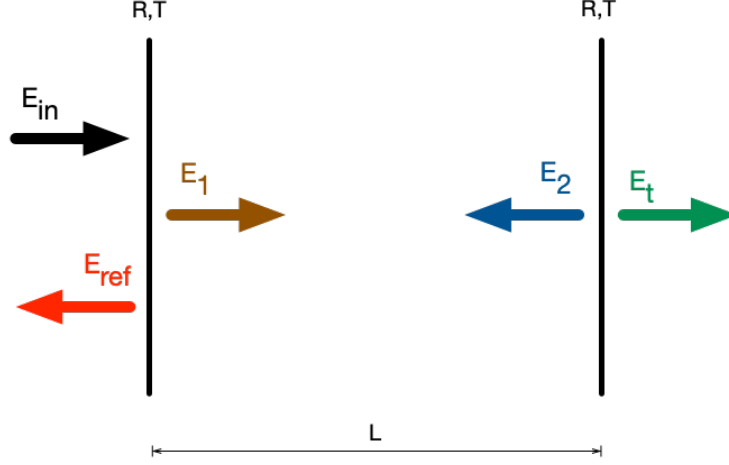


Figure 4.1: Schematic representation of a Fabry-Perot interferometer. E_{in} is the incident electric field, E_{ref} is the reflected electric field, E_t is the transmitted electric field, E_1 is the intra-cavity electric field propagating from left to right, E_2 is the intra-cavity electric field propagating from right to left, R and T are the reflectivity and transmissivity of the two identical mirrors and L is the distance between them.

In figure 4.2, the transmissivity (right) and reflectivity (left) of a lossless FP can be viewed. These graphs exhibit peaks with a periodicity equal to the FSR in the spectral domain. Recalling that $\text{FSR} = c/(2nL)$, one can see that the FSR is linked to the length of the cavity, with c the speed of light and n the refractive index of the medium that could be present between the two mirrors (nL is the optical path length). The finesse \mathcal{F} is related to the width of the peaks and depends on the reflectivity of the mirrors as $\mathcal{F} = 4R/(1 - R)^2$. As the reflectivity of the mirrors approaches 1, the finesse becomes large, and the peaks get narrow. On the other hand, with a lower reflectivity, more energy can leak out of the cavity even outside the resonance condition. Seeing the broadening of the peaks as energy leakage will be useful when drawing a parallel between FP and ring cavity interferometers.

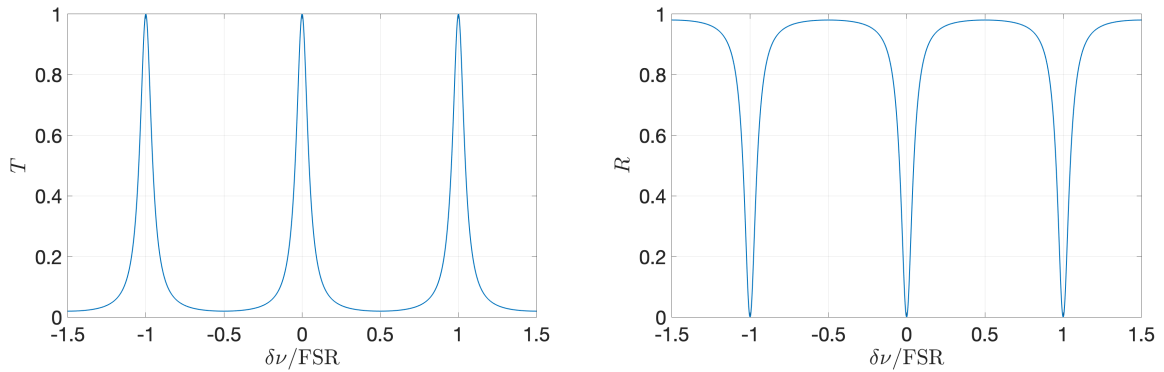


Figure 4.2: Transmissivity \mathcal{T} (left) and reflectivity \mathcal{R} (right) of the cavity. Finesse $\mathcal{F} = 50$. $\delta\nu$ denotes the deviation from a resonant frequency.

Equation (4.1) and (4.2) indicate that \mathcal{T} and \mathcal{R} depend on ω/FSR . This value can be rearranged as:

$$\frac{\omega}{\text{FSR}} = kL = \phi \quad (4.3)$$

Where k is the wave number defined as $n\omega/c$ and ϕ is the phase acquired by the electric field when propagating along the cavity. Therefore, by measuring the transmitted or reflected power, one can gain information about the phase (modulo π , because the periodicity of \mathcal{T} and \mathcal{R} in the phase domain is π) of the electric field. This is the idea underlying interferometry.

4.1.2 Ring cavity

A ring cavity exhibits the same behaviour as a FP interferometer. The structure of a ring cavity interferometer is displayed in figure 4.3. This is a fibre-based setup in which the incident electric field E_{in} penetrates the cavity from the left through a coupler. E_{ref} denotes the electric field exiting the cavity and E_1 and E_2 refer to the fields entering and leaving the fibre loop, respectively. The nomenclature for the fields was chosen in such a way that the analogy with the FP cavity can be understood. Indeed, one could see the coupler acting as the leftmost mirror from the figure 4.1, and the fibre loop as the one on the right side because it turns E_1 into E_2 and dissipates energy through fibre losses, whereas for the mirror it was by leakage out of the lossless FP cavity.

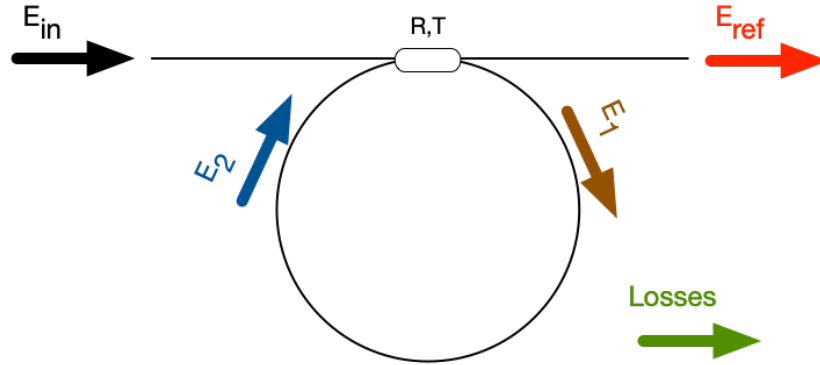


Figure 4.3: Schematic view of a ring cavity.

Because of the similarities between ring cavities and FPs, the former show the same transmissivity and reflectivity as the latter. Therefore, by measuring the reflected power, one can determine the phase acquired by the electric field inside the cavity.

4.1.3 Interferometric properties of the reservoir cavity

The basic principle of interferometry has been introduced through the presentation of the FP interferometer, and in the discussion that followed, it has been shown that a ring cavity, such as the reservoir cavity studied in this thesis, can be used as an interferometer. Moreover, it has also been shown that \mathcal{R} depends on the frequency (or wavelength) and on the length of the cavity and that the phase acquired by the incident electric field after one round trip could be determined by studying the reflected power.

In the reservoir cavity, many different wavelengths coexist because they encode the different neurons. Furthermore, after each round trip, the respective phase acquired by

each neuron should be a constant, as shown on equation (3.9). Recalling the phase matrix Φ defined in equation (3.8), the phase factor multiplying the k^{th} neuron is given by $\Phi_{kk} = \exp(i\phi_k)$. The phase ϕ_k is given by:

$$\phi_k = \beta(\omega + k\Omega)L \quad (4.4)$$

With β the fibre wave number, $\omega + k\Omega$ the angular frequency of the k^{th} neuron and L the length of the fibre loop. Because $k\Omega \ll \omega$, the wave number can be Taylor expanded:

$$\beta(\omega + k\Omega) = \beta(\omega) + \left. \frac{\partial \beta}{\partial \omega} \right|_{\omega} k\Omega + \mathcal{O}((k\Omega)^2) \quad (4.5)$$

By rewriting $\beta(\omega)$ and $\partial\beta/\partial\omega|_{\omega}$ as β_0 and β_1 , respectively, as it is often done in the literature, the acquired phase is given by:

$$\phi_k \approx \beta_0 L + k\beta_1 \Omega L = \phi_0 + k\phi_1 \quad (4.6)$$

This means that if ϕ_1 is an integer multiple of π , the phase factor multiplying all the neurons will be the same up to a sign:

$$e^{i(\phi_0 + k\phi_1)} = e^{i\phi_0} e^{ikm\pi} = (-1)^{km} e^{i\phi_0}, \quad m \in \mathbb{Z} \quad (4.7)$$

A periodicity of π and not 2π is considered here, because as claimed before, an interferometer can only inform about a phase modulo π . Looking for an acquired phase equal to π is the approximately the same as taking a modulation frequency Ω for the PM which is an integer multiple of the FSR. Indeed, by considering $\beta_1 \approx n/c$, one can find:

$$\beta_1 \Omega L \approx \frac{\Omega n L}{c} = m\pi \longrightarrow \Omega \approx \frac{m\pi c}{nL} = m2\pi \text{ FSR} \quad (4.8)$$

This is a legitimate assumption given the fact that in the region of interest the curve of $\beta(\omega)$ computed using the Sellmeier relations [7, 28] exhibits negligible nonlinearity.

It is not critical to modulate the phase at an angular frequency Ω which is an integer multiple of the FSR, the reservoir can in fact operate in different regimes. Those considerations were presented to better understand the physics underlying the phase management of the reservoir.

To be able to function as a RC, the reservoir has to be stabilised because during its operation, perturbations coming from various sources, such as mechanical constraints or temperature changes for example, can induce a phase fluctuation, which affects the RC performances. Classical cavity stabilisation strategies rely on interferometric properties to ensure the regulation. They use Proportional-Integral-Derivative (PID) regulators to maintain the reflected power at a reference level, which can be related to a phase, knowing the reflectivity of the cavity. A technical issue inherent to this scheme is the fact that the incident electric field used to stabilise the cavity is also modulated in intensity because it is carrying the input data processed by the RC, which has the consequence of deteriorating the reflected power signal based on which the cavity is stabilised. A possible solution is to use the Pound-Drever-Hall (PDH) stabilisation technique, which is an advanced cavity stabilisation technique leading to better performances. These two stabilisation techniques are presented in sections 4.4.1 and 4.4.2, respectively.

4.2 Experimental setup

In this section, the experimental setup employed to physically implement the WDM PRC is presented. First, it is detailed based with the help of the schematic representation of figure 4.4. Then, technical data about the devices involved in the experiment are given.

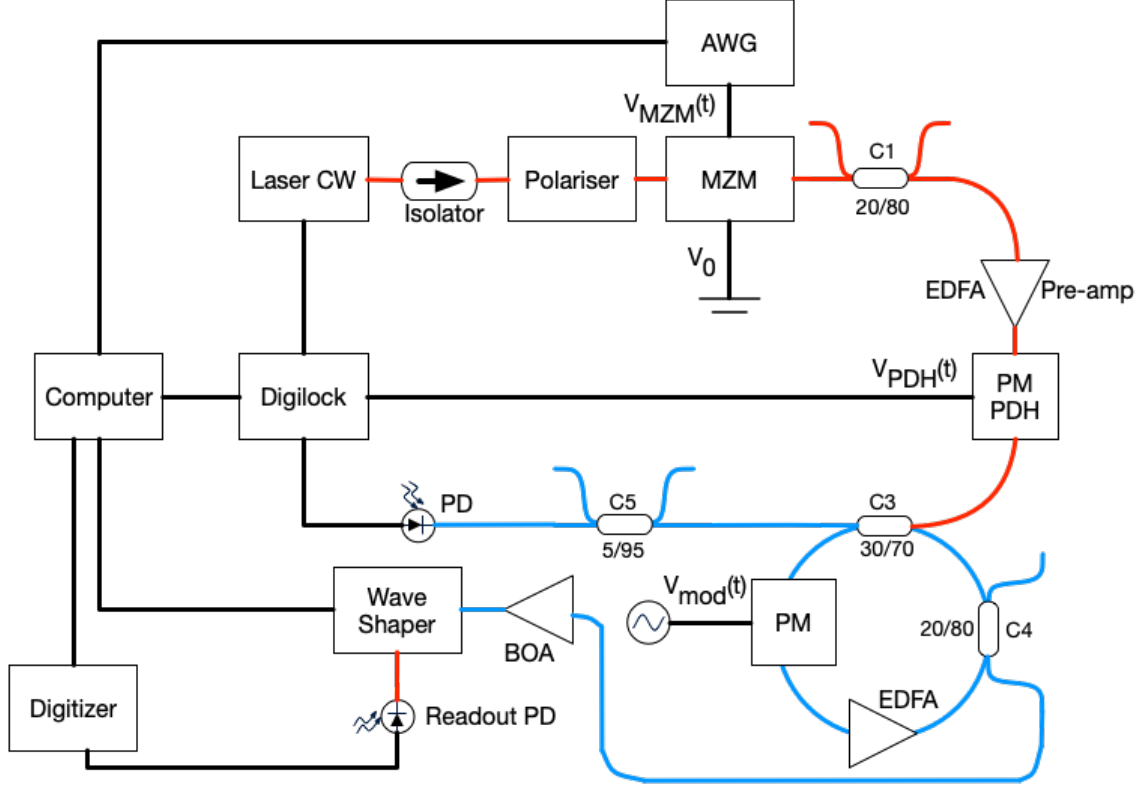


Figure 4.4: Schematic representation of the experimental setup. Red and blue lines: polarisation maintaining single mode fibres with only one or several wavelengths coexisting, respectively, black lines: electrical connections, CW: continuous wave, AWG: arbitrary wave generator, MZM: Mach-Zehnder Modulator, EDFA: Erbium Doped Fibre Amplifier, PM: phase modulator, PM - PDH, phase modulator involved in the PDH technique, PD: photodiode, C_x : coupler number x , BOA: Booster Optical Amplifier.

The setup presented here is mostly an update on the one presented in [1]. In figure 4.4, electrical wires and single mode polarisation maintaining fibres are represented using black and coloured lines, respectively. The light source of the setup is a narrow band continuous laser, which sends a single wavelength $\lambda_0 = 1555$ nm to the reservoir. The light goes through an isolator that prevents any backward reflection towards the laser source and then enters a polariser that ensures that only one linear polarisation mode is present inside the setup. This needs to be done to avoid any potential coupling between the two polarisation modes, and because the optoelectronic devices involved in the experiment, such as the MZM and the PMs, are polarisation dependent. The electric field then enters the MZM which is driven by the time dependent voltage $V_{\text{MZM}}(t)$. This signal is generated by an Arbitrary Wave Generator (AWG) based on the input time series $u(n)$ sent by the computer running the experiment. Since the transfer function of the MZM is nonlinear, the signal V_{MZM} can be precompensated in order to counteract the nonlinearity. Without precompensation, the voltage $V_{\text{MZM}}(t)$ is simply given by $\beta \tilde{u}(t)$, with β the input gain $\in [0, 1]$ and $\tilde{u}(t)$ the *sample and hold* version of $u(n)$ already introduced in the previous chapter. A bias tension V_0 can also be applied to the MZM to

change its average transparency. The transfer function of the MZM is given by :

$$\sin \left(\frac{\pi}{2} \left(\frac{V_{\text{MZM}}(t)}{V_{\pi,\text{RF}}} + \frac{V_0}{V_{\pi,\text{DC}}} \right) \right) \quad (4.9)$$

With $V_{\text{MZM}} \in [-\beta V_{\pi,\text{RF}}, \beta V_{\pi,\text{RF}}]$, and $V_{\pi,\text{RF}}$ and $V_{\pi,\text{DC}}$ the dynamic and static characteristic voltages of the MZM, respectively. The modulated electric field is then pre-amplified using an Erbium-Doped Fibre Amplifier (EDFA), and undergoes a first phase modulation. This is required to be able to implement the PDH stabilisation technique. The PM is driven by the alternative voltage $V_{\text{PDH}} = A_{\text{PDH}} \sin(\Omega_{\text{PDH}} t)$ supplied by the *Toptica Digilock 110* feedback controller denoted "Digilock" on the figure. This device handles every aspect related to the stabilisation of the reservoir, which is why it needs to be connected to the photodiode "PD" and to the laser, which are both involved in the regulation of the cavity, as it is explained in section 4.4.1. The electric field then enters the reservoir through the coupler "C3". The reservoir cavity is made of the fibres of the different couplers and is around 18m long. At this point, the colour used to represent the optical fibres changes from red to blue to indicate that inside the reservoir, several wavelengths are present whereas before the coupler there was only one. Inside the reservoir, the PM is used to mix the different frequencies and is driven by an external alternative voltage $V_{\text{mod}}(t) = A_{\text{mod}} \sin(\Omega_{\text{mod}} t)$. To allow a clear distinction between the different sidebands without degrading the achievable modulation depth, the modulation frequency $\Omega_{\text{mod}}/2\pi$ is around 20 GHz. This allows the existence of 13 neurons inside the cavity (6 sidebands on both sides of the central frequency) with wavelengths going from 1.554 μm to 1.556 μm in the telecom C-band. The PM introduces insertion losses that are compensated using the EDFA, whose pump current is adjusted to tune the feedback gain α that appears in equation (3.9). The electric field exiting the reservoir at the level of the coupler "C3" towards the photodiode "PD" is the reflected field, according to what was discussed in section 4.1.2. The electric field finally illuminates the photodiode "PD", and produces a voltage proportional to its intensity, called the reflected power. This measured signal enters the Digilock where it is used electronically post-processed in order to recover the PDH signal, whose properties are presented in section 4.4.2. Based on the value of this signal, the Digilock outputs a control voltage that is applied to a piezo-electric crystal inside the laser cavity and that modifies its emission wavelength. The output of the reservoir exits the cavity through the coupler "C4" and is amplified by a SOA called "BOA" for Booster Optical Amplifier to improve the SNR. A demultiplexing scheme allowing to obtain the value of each individual neuron at the same time has not been implemented yet. To overcome this limitation, the adjustable band-pass filter denoted "Wave Shaper" is used to record the evolution of only one neuron at a time. This implies that if one wants to compute the output of the reservoir $y(n)$, one has to run the same experiment once for each of the neuron, to program the Wave Shaper to filter out all the other sidebands and to save its evolution on the computer. Once this has been done, $y(n)$ can be reconstructed. As far as the learning procedure is concerned, it follows the same procedure as the one previously described, but modified to take this sequential measurements of the neurons into account. In terms of the devices used to perform this task, the photodiode "Readout PD" measures the intensity of each of the filtered neuron, and the "Digitizer" handles the conversion between continuous time dependent signals into time series usable by the computer. To conclude this description of the experimental setup, one should note that the couplers "C1" and "C5" are used in practice to monitor the electric fields when modifications are made to the optical table, and that the AWG, Digilock, Wave Shaper and Digitizer are all controlled by the computer. The technical specifications of the devices used in the experiment can be found in appendix B.

4.3 Characterisation of the reservoir

To be able to develop a reliable stabilisation scheme for the reservoir, some of its characteristics need to be studied as a preliminary work. First, one can gain important insights by modelling the transfer function of the reservoir. In this context, the transfer function is simply the reflectivity of the cavity as a function of the frequency of the incident wave. However, given the fact that the reservoir is a more complex ring cavity than the one depicted in section 4.1.2, it will not exhibit the same behaviour as the one of a FP cavity as displayed in figure 4.2. A mathematical model is first derived and the results it provides are compared to experimental transfer functions. After that, the experimental study of the effective losses is tackled. The effective losses are used in the model to take into account the fibre losses, the insertion losses of the PM and the gain of EDFA using only one factor. Finally, an empirical relation between the modulation amplitude driving the intra-cavity PM and its modulation depth is determined experimentally.

4.3.1 Transfer function of the cavity

As already claimed, in the context of cavity stabilisation, the transfer function is the reflectivity. When operating the reservoir, the reflected power which is proportional to the intensity of the electric field reflected by the cavity gives an indication on the phase of the field inside it, which implies that the regulation procedure relies on the measurement of this signal.

In figure 4.5, the reservoir is represented with the different electric fields that turn out to be useful when studying the transfer function. The colour code for the fibres is the same as the one used previously. The incident electric field \mathbf{E}_{in} enters the cavity through a coupler from the top left optical fibre. Inside the cavity, it is amplified by the EDFA and then is phase modulated. After that, a portion of the electric field exits the cavity through the coupler C4 to be read out. The light inside the cavity finally terminates its round trip.

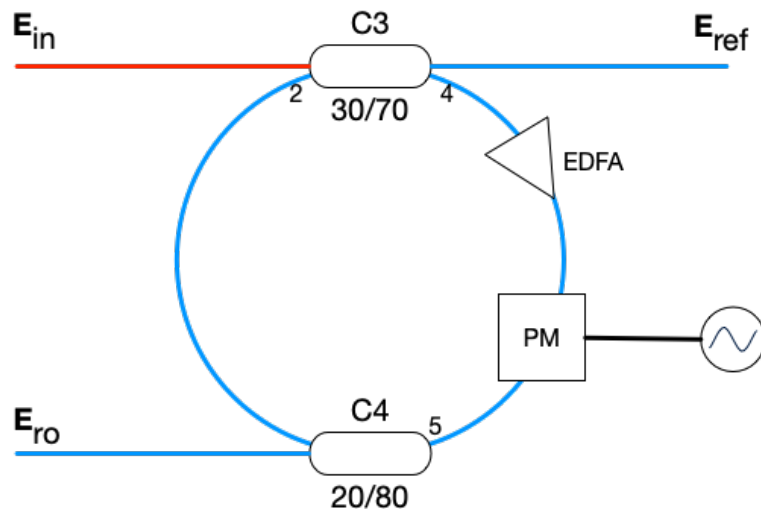


Figure 4.5: Schematic representation of the reservoir.

Mathematical model

In this section, a mathematical model for the transfer function is derived. To do so, the formalism introduced in section 3.1.3 needs to be used. This can be done because the basis vectors were chosen such that a neuron state vector \mathbf{x} is formally equal to an electric field. Therefore, one should pay attention to the fact that when referring the a vectorial electric field \mathbf{E} , it denotes an electric field expressed in the abstract basis $\{\hat{\mathbf{e}}_j | \hat{\mathbf{e}}_j = \exp(i(\omega + j\Omega_{\text{mod}}t)), j \in [-\eta, \eta]\}$ instead of the usual physical space $\{\mathbf{1}_x, \mathbf{1}_y, \mathbf{1}_z\}$. It is recalled that $\eta = \lfloor N/2 \rfloor$ is the variable introduced to iterate through through the neurons in more convenient way.

The transfer function \mathbf{R} is defined as the link between the incident and reflected electric fields:

$$\mathbf{E}_{\text{ref}} = \mathbf{R} \mathbf{E}_{\text{in}} \quad (4.10)$$

Given the vectorial nature of \mathbf{E}_{ref} and \mathbf{E}_{in} , the transfer function is in fact a transfer matrix in this particular context. Recalling that the laser only emits light at the center wavelength, the incident field \mathbf{E}_{in} is given by:

$$\mathbf{E}_{\text{in}} = E_0 \hat{\mathbf{e}}_0 \quad (4.11)$$

With E_0 being an arbitrary complex amplitude. Given the properties of the coupler C3, one finds:

$$\begin{bmatrix} \mathbf{E}_{\text{ref}} \\ \mathbf{E}_4 \end{bmatrix} = \begin{bmatrix} \varepsilon_1 & i\sqrt{1-\varepsilon_1^2} \\ i\sqrt{1-\varepsilon_1^2} & \varepsilon_1 \end{bmatrix} \begin{bmatrix} \mathbf{E}_{\text{in}} \\ \mathbf{E}_2 \end{bmatrix} \quad (4.12)$$

Which yields to the following expression for the reflected field:

$$\mathbf{E}_{\text{ref}} = \varepsilon_1 \mathbf{E}_{\text{in}} + i\sqrt{1-\varepsilon_1^2} \mathbf{E}_2 \quad (4.13)$$

Let us now express \mathbf{E}_2 as a function of \mathbf{E}_{in} to close the system. Using the transfer matrix of the coupler C4, \mathbf{E}_2 reads :

$$\begin{bmatrix} \mathbf{E}_2 \\ \mathbf{E}_{\text{ro}} \end{bmatrix} = e^{-\gamma L} \begin{bmatrix} \varepsilon_2 \\ \sqrt{1-\varepsilon_2^2} \end{bmatrix} \mathbf{E}_5 \implies \mathbf{E}_2 = \varepsilon_2 e^{-\gamma L} \mathbf{E}_5 \quad (4.14)$$

With γ the effective losses coefficient and L , the length of the reservoir. Since the system is in a linear regime, the position of the coupler C4 in the cavity has no influence on the losses and on the phase. This property manifests itself because mathematically, the transfer matrix of the coupler C4 and the phase matrix Φ commute. By defining $\xi \in [0, 1]$ as the variable indicating the relative position of the PM inside the cavity ($\xi = 0$ if it is at the beginning of the cavity, $\xi = 1$ if it is at the end). The phase acquired by the electric field inside the reservoir is now dependent on the position of the PM. This leads to the definition of two new matrices Φ_ξ and $\Phi_{1-\xi}$, which are based on the phase matrix Φ . They are diagonal matrices, expressed as:

$$\begin{aligned} \Phi_{\xi,nn} &= \exp(i\beta(\omega + n\Omega_{\text{mod}})\xi L) \\ \Phi_{1-\xi,nn} &= \exp(i\beta(\omega + n\Omega_{\text{mod}})(1-\xi)L) \end{aligned} \quad (4.15)$$

With $\beta(\omega + n\Omega_{\text{mod}})$ the dispersion relation of the fibre evaluated at the frequency of the n^{th} neuron. Recalling the coupling matrix of the PM \mathbf{J} , one can rewrite \mathbf{E}_5 as a function of \mathbf{E}_4 :

$$\mathbf{E}_5 = \Phi_{1-\xi} \mathbf{J} \Phi_\xi \mathbf{E}_4 \quad (4.16)$$

Using the transfer matrix of the coupler C3, one can express \mathbf{E}_4 as a function of \mathbf{E}_{in} and \mathbf{E}_2 :

$$\mathbf{E}_4 = i\sqrt{1 - \varepsilon_1^2} \mathbf{E}_{\text{in}} + \varepsilon_1 \mathbf{E}_2 \quad (4.17)$$

This yields to a closed equation to determine \mathbf{E}_2 :

$$\begin{aligned} \mathbf{E}_2 &= i\sqrt{1 - \varepsilon_1^2} \varepsilon_2 e^{-\gamma L} \Phi_{1-\xi} \mathbf{J} \Phi_\xi \mathbf{E}_{\text{in}} + \varepsilon_1 \varepsilon_2 e^{-\gamma L} \Phi_{1-\xi} \mathbf{J} \Phi_\xi \mathbf{E}_2 \\ \hookrightarrow \mathbf{E}_2 &= i\sqrt{1 - \varepsilon_1^2} \varepsilon_2 e^{-\gamma L} (\mathbf{I} - \varepsilon_1 \varepsilon_2 e^{-\gamma L} \Phi_{1-\xi} \mathbf{J} \Phi_\xi)^{-1} \Phi_{1-\xi} \mathbf{J} \Phi_\xi \mathbf{E}_{\text{in}} \end{aligned} \quad (4.18)$$

Now that \mathbf{E}_2 has been determined, it is easy to compute \mathbf{E}_{ref} using equation (4.13):

$$\begin{aligned} \mathbf{E}_{\text{ref}} &= \varepsilon_1 \mathbf{E}_{\text{in}} - (1 - \varepsilon_1^2) \varepsilon_2 e^{-\gamma L} (\mathbf{I} - \varepsilon_1 \varepsilon_2 e^{-\gamma L} \Phi_{1-\xi} \mathbf{J} \Phi_\xi)^{-1} \Phi_{1-\xi} \mathbf{J} \Phi_\xi \mathbf{E}_{\text{in}} \\ \hookrightarrow \mathbf{E}_{\text{ref}} &= (\varepsilon_1 \mathbf{I} - (1 - \varepsilon_1^2) \varepsilon_2 e^{-\gamma L} (\mathbf{I} - \varepsilon_1 \varepsilon_2 e^{-\gamma L} \Phi_{1-\xi} \mathbf{J} \Phi_\xi)^{-1} \Phi_{1-\xi} \mathbf{J} \Phi_\xi) \mathbf{E}_{\text{in}} \end{aligned} \quad (4.19)$$

This last equality reveals the expression of the transfer matrix \mathbf{R} :

$$\boxed{\mathbf{R} = \varepsilon_1 \mathbf{I} - (1 - \varepsilon_1^2) \varepsilon_2 e^{-\gamma L} (\mathbf{I} - \varepsilon_1 \varepsilon_2 e^{-\gamma L} \Phi_{1-\xi} \mathbf{J} \Phi_\xi)^{-1} \Phi_{1-\xi} \mathbf{J} \Phi_\xi} \quad (4.20)$$

Even if this result is interesting, it cannot be measured directly since it involves electric fields instead of intensities. What is measured using a PD is the reflectivity \mathcal{R} linking the incident intensity to the reflected intensity. Recalling that the incident electric field is given by $\mathbf{E}_{\text{in}} = E_0 \hat{\mathbf{e}}_0$, the reflected electric field is given by:

$$\mathbf{E}_{\text{ref}} = \mathbf{R} \mathbf{E}_{\text{in}} = E_0 \sum_{n=-\eta}^{\eta} R_{n,0} \hat{\mathbf{e}}_n \quad (4.21)$$

The sum in this formula is expressed using the numbering introduced in section 3.1.3 which is more natural for this kind of situation. As a reminder, instead of going through the indices from 1 to N , this alternative notation goes from $-\eta$ to η , with index 0 referring to the central neuron. Thus, the above equation basically means that \mathbf{E}_{ref} is equal to E_0 multiplying the central column of \mathbf{R} .

The reflected intensity is given by:

$$|\mathbf{E}_{\text{ref}}|^2 = |E_0|^2 \left(\sum_{n=-\eta}^{\eta} R_{n,0} \hat{\mathbf{e}}_n \right) \left(\sum_{m=-\eta}^{\eta} R_{m,0}^* \hat{\mathbf{e}}_m^* \right) \quad (4.22)$$

This expression seems complicated at first sight, but it can be simplified by putting forward an experimental argument. First, let us consider the product $\hat{\mathbf{e}}_n \cdot \hat{\mathbf{e}}_m^*$, which is equal to $\exp(i(n-m)\Omega_{\text{mod}}t)$. If $m = n$, then the product is equal to one and the term $|R_{n,0}|^2$ has to be taken into account in the sum. On the other hand, if $m \neq n$, then product corresponds to a beating of the intensity at frequency $(n-m)\Omega_{\text{mod}}/2\pi$, which is an integer number of times approximately 20 GHz. However, as can be seen in the appendix B, the bandwidth of the PD is limited to 120 MHz. Therefore the PD is not able to resolve the beating waves, which implies that when $m = n$, the signals do not contribute to the sum. This yields to a simplified version of the reflected intensity:

$$|\mathbf{E}_{\text{ref}}|^2 = |E_0|^2 \sum_{n=-\eta}^{\eta} |R_{n,0}|^2 \quad (4.23)$$

The reflectivity of the reservoir is finally given by:

$$\mathcal{R} = \sum_{n=-\eta}^{\eta} |R_{n,0}|^2 \quad (4.24)$$

Note that this model is solely valid when considering the evolution of the reservoir at time scales much larger than $2\pi/\text{FSR}$. This assumption ensures that one is working in a stationary regime with respect to the characteristic time-scale of the reservoir.

Experimental results

The adequacy of the analytical model just derived is assessed by comparing its predictions to experimental data. To capture data concerning transfer functions, one performs a *sweep* using the Digilock. As already explained, the Digilock is connected to a piezoelectric crystal controlling the emission wavelength of the laser, whose shift is proportional to the applied tension. As a reminder, the transfer function is the reflectivity \mathcal{R} as a function of ω , therefore one needs to be able to scan the frequency domain. The sweep procedure allows to do it by applying a triangular periodic voltage to the piezoelectric, which leads to a proportional evolution of the emission wavelength of the laser. The frequency and amplitude of this signal are controlled by the Digilock interface. This procedure allows to plot the reflected power as a function of the time to observe its shape.

To relate the theoretical curves to raw data, one should express the link between the time and the angular frequency. Using a first order Taylor approximation, the angular frequency variation reads:

$$\delta\omega = -\frac{2\pi c}{\lambda_0^2} \delta\lambda \quad (4.25)$$

With λ_0 the central wavelength (1555 nm). In appendix B, one can find that the piezoelectric tuning characteristic is equal 0.1 pm/V at a sweeping frequency of 100 Hz. Let us denote this value by p and let us call q the slope of the triangular voltage as a function of the time, which depends on the settings of the sweep. Multiplying those two constants provides a proportionality indicating the range of wavelengths spanned per unit of time. This yields to a link between time and angular frequency:

$$\omega = -pq \frac{2\pi c}{\lambda_0^2} t \quad (4.26)$$

Below, comparisons between simulations and experimental data are shown for three different regimes. Since the theoretical reflectivity \mathcal{R} is a ratio, it is comprised between 0 and 1. Therefore, it had to be rescaled in order to be compared with the reflected powers measured by the PD.

First sideband at resonance If the central neuron is at resonance, this means that Ω_{mod} is chosen such that the first sideband is at resonance as well. In other words, $\Omega_{\text{mod}}/2\pi$ is an integer number of times the FSR of the cavity. This is displayed in figure 4.6.

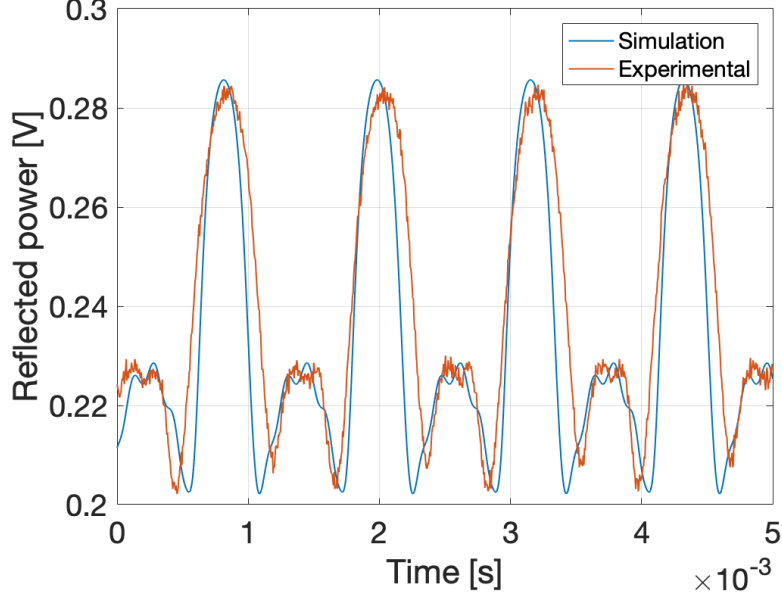


Figure 4.6: Reflected power [V] as a function of the time [s] during a sweep of the piezo voltage. First sideband at resonance. $\Omega_{\text{mod}} = 19.99$ GHz, modulation depth $m = 2$, $\gamma = 0.0126 \text{ m}^{-1}$. The theoretical curve has been rescaled in order to be compared with the experimental curve.

First sideband halfway between resonance and anti-resonance Ω_{mod} is tuned such that $\Omega_{\text{mod}}/2\pi$ is an odd number of times the quarter of the FSR. The experimental results are given on the figure 4.7.

First sideband at anti-resonance $\Omega_{\text{mod}}/2\pi$ is an odd number of times half of the FSR. The graphs are depicted on the figure 4.8.

On those graphs, one can see that the transfer function highly depends on the modulation frequency. Even though the experimental adequacy is not perfect, it is sufficient to have a qualitative idea of the behaviour of the reservoir. It also allows to experimentally deduce its FSR by measuring the temporal periodicity of the reflectivity, and then to translate in the frequency domain using equation (4.26).

$$\Delta t = 1.155 \text{ ms} \implies \text{FSR} \approx pq \frac{c}{\lambda_0^2} \Delta t \approx 11.5 \text{ MHz} \quad (4.27)$$

Recalling that the FSR for a ring cavity is given by:

$$\text{FSR} = \frac{c}{nL} \quad (4.28)$$

Using this formula, one can compute the length of the cavity: $L = 18.33 \text{ m}$.

As a final remark, the relative position of the PM inside the cavity (controlled using the variable ξ) does not seem to have an influence on the shape of the transfer function.

4.3.2 Effective losses

Given the model derived, the only physical quantity that cannot be known from a simple inspection of the data sheets are the effective losses γ . They arise due to the effects of the fibre losses, the insertion loss of the intra-cavity PM and the gain of the

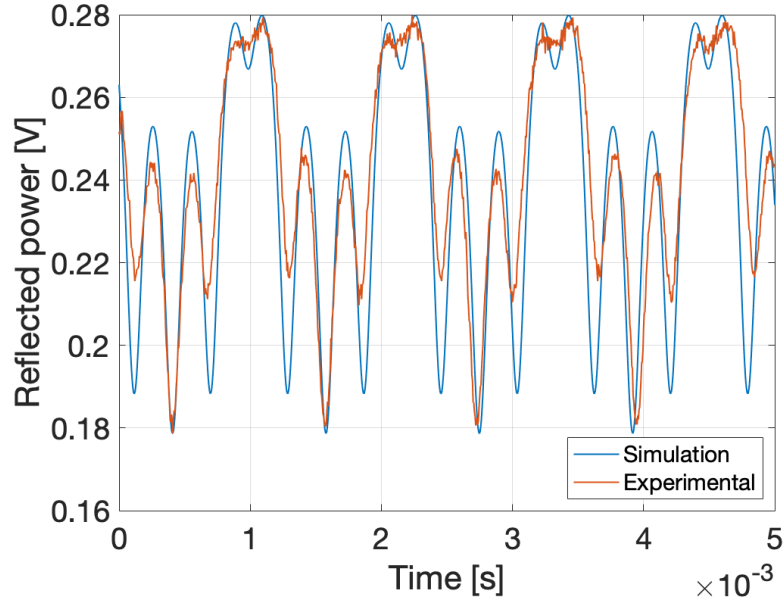


Figure 4.7: Reflected power [V] as a function of the time [s] during a sweep of the piezo voltage. First sideband halfway between resonance and anti-resonance. $\Omega_{\text{mod}} = 19.9997$ GHz, modulation depth $m = 2$, $\gamma = 0.0126 \text{ m}^{-1}$. The theoretical curve has been rescaled in order to be compared with the experimental curve.

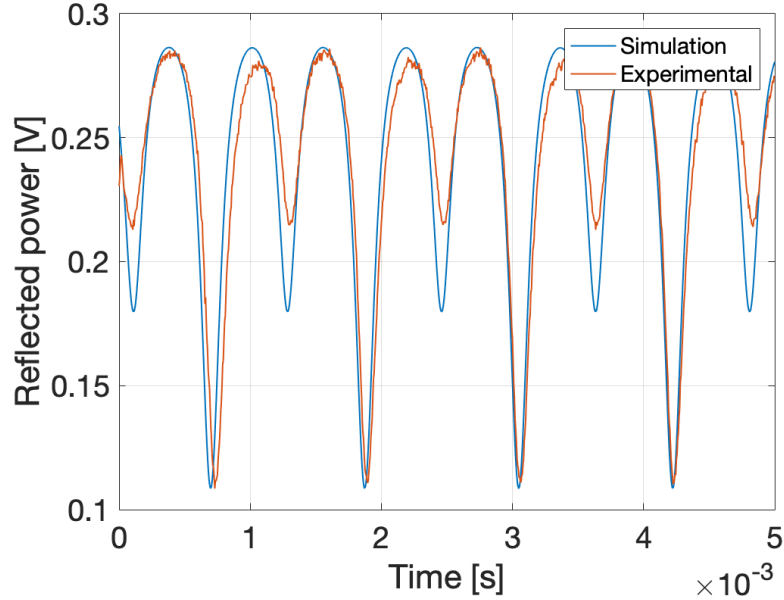


Figure 4.8: Reflected power [V] as a function of the time [s] during a sweep of the the piezo voltage. First sideband at anti-resonance. $\Omega_{\text{mod}} = 19.9997$ GHz, modulation depth $m = 2$, $\gamma = 0.0126 \text{ m}^{-1}$. The theoretical curve has been rescaled in order to be compared with the experimental curve.

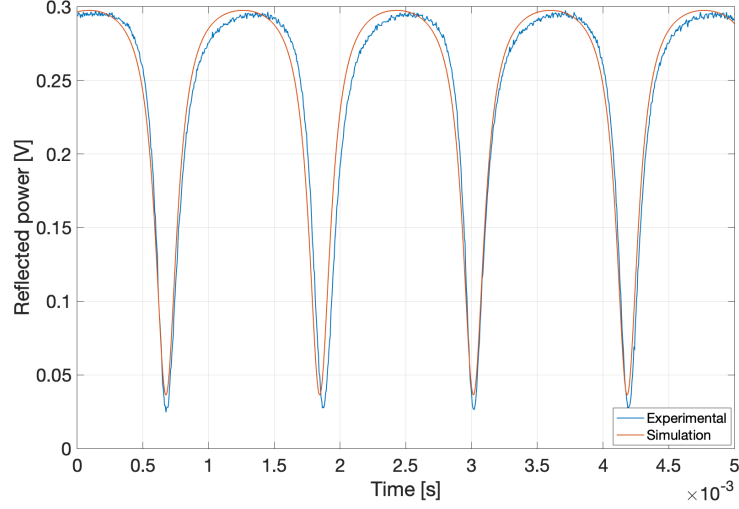


Figure 4.9: Reflected power [V] as function of the time [s] during a sweep of the the piezo voltage, no intra-cavity phase modulation, $\gamma = 0.0126 \text{ m}^{-1}$. The theoretical curve has been rescaled in order to be compared with the experimental curve.

EDFA. Their value is determined experimentally. To do so, a least square fit is performed. Basically, this means that one compares an experimental curve with an analytical one, for which the value of γ is not fixed. The deviation between those two curves is therefore a function of γ , and can be minimised. Mathematically speaking, the experimental effective losses $\tilde{\gamma}$ are given by:

$$\tilde{\gamma} = \underset{\gamma}{\operatorname{argmin}} \sum_{i=1}^T (\mathcal{R}_i - \mathcal{R}(t_i; \gamma))^2 \quad (4.29)$$

Where T is the total number samples, \mathcal{R}_i is the measured reflected power for the i^{th} sample and $\mathcal{R}(t_i; \gamma)$ is the theoretical rescaled reflectivity evaluated at $t = t_i$ and γ , which is the time corresponding to the i^{th} sample and the effective losses, respectively. In figure 4.9, one can see the result of this optimisation. It was performed on the reservoir without phase modulation because it is assumed that the insertion losses do not depend on whether a phase modulation is going on. The effective losses that were determined using this procedure read:

$$\gamma = 0.0126 \text{ m}^{-1} \quad (4.30)$$

4.3.3 Modulation depth

When one wants to modify the modulation depth during a phase modulation process, one has to change the modulation power of the RF generator. The goal of this section is to determine an empirical relation linking the modulation power, expressed in dBm, and the modulation depth. The procedure to compute it is the following: one applies a methodology similar to the one from the previous chapter, except that instead of optimising for γ , one should do it for m , the modulation depth. This procedure is repeated several times, for different modulation powers, in order to form a data set. Finally, when one has gathered enough data, one can perform a polynomial interpolation that provides the link between the power and the depth that one was looking for. This method works better when one is working in the situation where the first sideband is at anti-resonance,

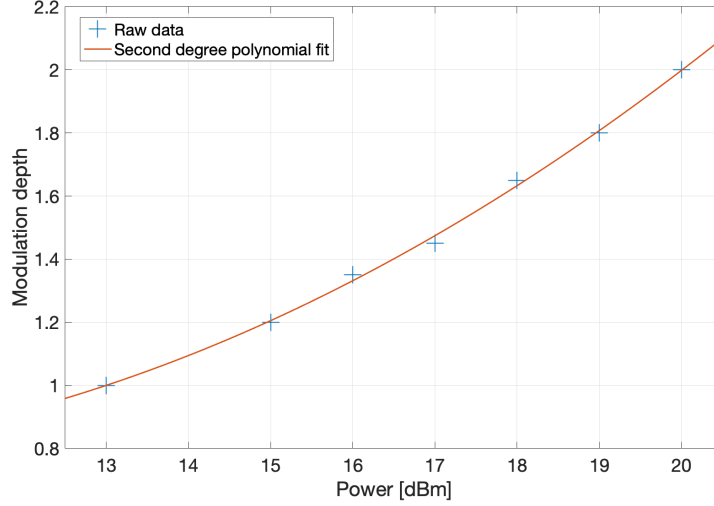


Figure 4.10: Modulation depth m as a function of the modulation power [dBm] and second degree polynomial interpolation for $\Omega_{\text{mod}}/2\pi = 19.9943$ GHz.

because in this regime, the depth of the side peaks (see figure 4.8) depends a lot on the modulation depth.

In figure 4.10, one can see the data, as well as the second degree polynomial interpolation. The experimental points only start at 13 dBm because below this value, the side peak was too small to lead significant measures. As already claimed, one cannot go above $m = 2$ experimentally without external amplification because the RF generator is not able to supply modulation powers higher than 20 dBm at such high modulation frequencies. The empirical polynomial relation is:

$$m(P[\text{dBm}]) = 8.004 \times 10^{-3} P^2[\text{dBm}] - 0.1215 P[\text{dBm}] + 1.222 \quad (4.31)$$

It is observed that higher orders can be neglected in the polynomial interpolation.

4.4 Pound-Drever-Hall stabilisation technique

In this section, the PDH stabilisation technique is presented. First, the rationale behind its introduction is discussed. After that, it is shown that the error function resulting from the PDH modulation reveals new informations about the phase of the electric field inside the cavity that allow to reach better stabilisation performances. Finally, a few remarks are given regarding the implementation of this scheme for the reservoir cavity.

4.4.1 Introduction

The PDH stabilisation technique was proposed in 1983 in [14] and since then has proven to be a powerful scheme enabling to accurately stabilise optical cavities. Among other applications, it has been used to stabilise the laser and measure the thermal noise in the arms of the Michelson interferometer of the LIGO [6], which made possible the observation of gravitational waves.

The basic idea of the PDH technique is to modify the transfer function of the cavity in such a way that its observation will provide more information about the phase. This is

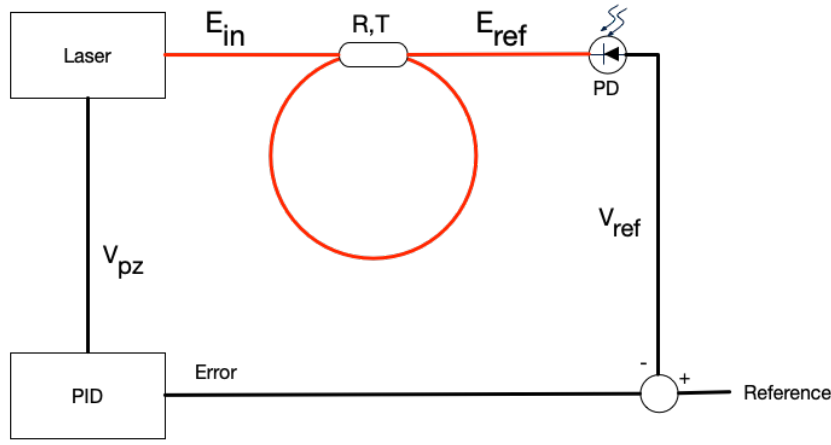


Figure 4.11: Schematic representation of a cavity being stabilised using the classical stabilisation technique. The red lines are optical fibres and the black ones are electrical connections.

implemented in practice by using an additional PM and some electronic post-processing, which is handled by the Digilock in our setup.

Cavity stabilisation

Before discussing the PDH scheme, the principles of classical cavity stabilisation are presented. As a reminder, this action consists of keeping the relative phase between the electric field inside the cavity after a round trip and the incident electric field equal to a constant value by maintaining the reflected power equal to the value translating to this relative phase using the transfer function. The reflected power of the cavity is measured using PDs, and can be modified by using actuators to change either the length of the cavity, or the emission wavelength of the laser.

In figure 4.11, one can observe the basic principle of the regulation of an optical cavity. The top branch of the figure is well-known at this point. The incident field E_{in} enters the cavity at the level of the coupler, where the reflected E_{ref} exits the cavity. The latter is then measured by the PD. Henceforth, the different elements should be looked at under the light of control theory. The measured voltage V_{ref} is compared to a reference, which is the value that the regulator is trying to maintain. The difference between the reference and the measured voltage is the so-called error, which is processed by a device named the PID regulator. In all generality, a PID regulator, or PID in short, is governed by this equation in the time domain [17, p.196]:

$$u(t) = k_P e(t) + k_I \int_{-\infty}^t e(\tau) d\tau + k_D \frac{de}{dt}(t) \quad (4.32)$$

With $u(t)$ the output of the PID, which is in this context the voltage applied to the piezoelectric V_{pz} , $e(t)$ the error and k_I , k_P and k_D the proportional, integral, and differential coefficients, respectively. In order to get the PID to work, one needs to tune those three coefficients, either using analytical methods, or heuristically by scanning the different values. The latter option was the one followed in the experimental implementations described in this work.

The voltage V_{pz} , the output of the PID, is applied to the piezoelectric crystal of the laser and alters its emission wavelength to stay synchronised with the reference.

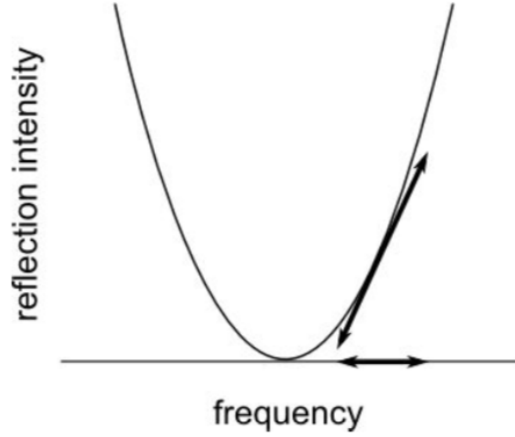


Figure 4.12: Schematic graph of the transfer function \mathcal{R} near a resonance as function of the frequency [32].

The main limitation of this scheme is linked to the symmetry of the transfer function \mathcal{R} . Let us illustrate why the symmetry is a shortcoming by considering a specific situation, with the help of the figure 4.12. Let us assume an initial condition when one has a cavity stabilised at the resonance, namely at the minimum of the curve. If the cavity is disturbed by any kind of perturbations, the reflected signal will increase, but due to the symmetry with respect to the resonance frequency, how will one know if the phase is increasing or decreasing ? The measured signal will be exactly the same in both situations. This is problematic because instead of rejecting the perturbations, the PID could amplify them by interpreting the measured signal in the wrong way. A trick to still be able to stabilise a cavity using this method is to consider not only the instantaneous value of the reflected signal, but also its slope. Doing so, one is able to differentiate between a larger (positive slope) or smaller (negative slope) frequency. Yet, this workaround is not recommended because it is more convenient to work only with instantaneous signals. The PDH technique overcomes this limitation by introducing a transfer function, called the error function, which is antisymmetric with respect to the resonance frequencies.

4.4.2 Pound-Drever-Hall scheme

The PDH stabilisation technique relies on the addition of a PM and electronic post-processing, as can be viewed in figure 4.13. The light sent by the laser goes through a PM driven by an AC voltage at frequency $\Omega_{\text{PDH}}/2\pi$ emitted by a RF generator. The modulation depth is chosen in such a way that all the sidebands but the first are negligible (one sideband on each side of the carrier frequency). Therefore, the electric field incident on the cavity E_{in} reads:

$$E_{\text{in}} = E_0 \left(J_0(m)e^{i\omega t} + J_1(m)e^{i(\omega+\omega_{\text{PDH}})t} - J_1(m)e^{i(\omega-\omega_{\text{PDH}})t} \right) \quad (4.33)$$

Given the fact that the cavity is linear, one can assume that its transfer function¹ R is linear as well, which gives for the reflected field E_{ref} :

¹As a reminder, the transfer function is the function such that $|R|^2 = \mathcal{R}$

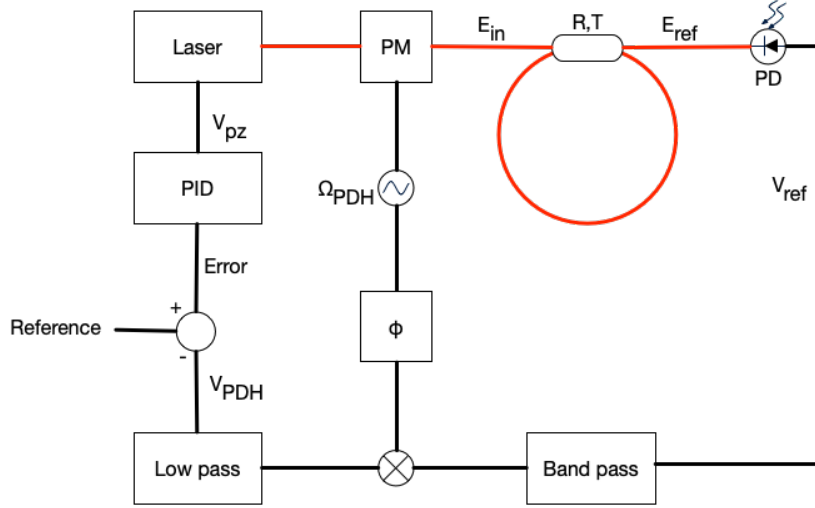


Figure 4.13: Schematic representation of a cavity being stabilised using the PDH technique. This schematic is based on the original blueprint presented in [14]. The colour convention for the lines is the same as in the previous figures. The phase of the light incident on the cavity is modulated by a PM driven by a local oscillator. The reflected power undergoes a band pass filtering, a mixing with the signal of the local oscillator shifted by a phase ϕ and a low pass filtering. The PDH error function is denoted by V_{PDH} . It is compared to a reference level to provide an error signal to the PID.

$$E_{\text{ref}} = E_0(J_0(m)R(\omega)e^{i\omega t} + J_1(m)R(\omega + \Omega_{\text{PDH}})e^{i(\omega + \Omega_{\text{PDH}})t} - J_1(m)R(\omega - \Omega_{\text{PDH}})e^{i(\omega - \Omega_{\text{PDH}})t}) \quad (4.34)$$

The voltage at the PD is proportional to the intensity:

$$V_{\text{ref}} \propto |E_0|^2 \left(J_0^2(m)\mathcal{R}(\omega) + J_1^2(m)(\mathcal{R}(\omega + \Omega_{\text{PDH}}) + \mathcal{R}(\omega - \Omega_{\text{PDH}})) + 2J_0(m)J_1(m)\text{Re}[R(\omega)R^*(\omega + \Omega_{\text{PDH}}) - R^*(\omega)R(\omega - \Omega_{\text{PDH}})]\cos(\Omega_{\text{PDH}}t) + 2J_0(m)J_1(m)\text{Im}[R(\omega)R^*(\omega + \Omega_{\text{PDH}}) - R^*(\omega)R(\omega - \Omega_{\text{PDH}})]\sin(\Omega_{\text{PDH}}t) + \text{terms at } 2\Omega_{\text{PDH}} \right) \quad (4.35)$$

This signal goes to a band pass filter centred at Ω_{PDH} in order to remove the DC component and the terms oscillating at $2\Omega_{\text{PDH}}$. Let us define $\zeta(\omega)$ as:

$$\zeta(\omega) = R(\omega)R^*(\omega + \Omega_{\text{PDH}}) - R^*(\omega)R(\omega - \Omega_{\text{PDH}}) \quad (4.36)$$

The voltage at the output of the band pass filter reads:

$$V_{\text{BP}} \propto \text{Re}[\zeta(\omega)]\cos(\Omega_{\text{PDH}}t) + \text{Im}[\zeta(\omega)]\sin(\Omega_{\text{PDH}}t) \quad (4.37)$$

After that, the signal is mixed with the local oscillator driving the PM, shifted by an additional phase ϕ . A mixer is basically a nonlinear electronic device that multiplies two signals. Multiplying V_{BP} by $\sin(\Omega_{\text{PDH}}t + \phi)$ leads to a DC component, which contains the information one is trying to extract, and to a $2\Omega_{\text{PDH}}$ component. At this point, one

only has to use a low pass filter to retrieve the signal [32]. Recalling two trigonometric identities:

$$\cos(\Omega_{\text{PDH}}t) \cdot \sin(\Omega_{\text{PDH}}t + \phi) = \frac{1}{2}(\cos(2\Omega_{\text{PDH}}t + \phi) + \sin(\phi)) \quad (4.38)$$

$$\sin(\Omega_{\text{PDH}}t) \cdot \sin(\Omega_{\text{PDH}}t + \phi) = \frac{1}{2}(-\cos(2\Omega_{\text{PDH}}t + \phi) + \cos(\phi)) \quad (4.39)$$

One can see that multiplying V_{BP} by $\sin(\Omega_{\text{PDH}}t + \phi)$ and then low pass filtering yields to the following expression for V_{PDH} :

$$V_{\text{PDH}} \propto \text{Re}[\zeta(\omega)] \sin(\phi) + \text{Im}[\zeta(\omega)] \cos(\phi) \quad (4.40)$$

One can therefore select which component to use by changing the value of ϕ . The PDH error function $\varepsilon(\omega)$ is defined as:

$$\varepsilon(\omega) = \text{Im}[\zeta(\omega)] \quad (4.41)$$

The graph of the PDH error function is depicted on the right side of figure 4.14. As required, it is antisymmetric with respect to the resonance frequency, which allows to immediately differentiate between an increase or a decrease of phase. Moreover, thanks to the steep slope of the curve at resonance, a small variation of phase implies a large variation of ε . On the right side of the figure, one can see that $\text{Re}[\zeta]$ provides no useful information about the phase, which is why it is not used in practice.

The end of the regulation scheme is the same as the previous one. The PDH signal V_{PDH} (with $\phi = 0$) is compared to a reference, which gives the error, and this error is used by the PID to regulate the laser. This scheme can stabilise the cavity at any phase, provided that the slope on the neighbourhood of this phase is steep enough. This condition being quite vague, it should be checked experimentally whether it is possible to stabilise at a given phase.

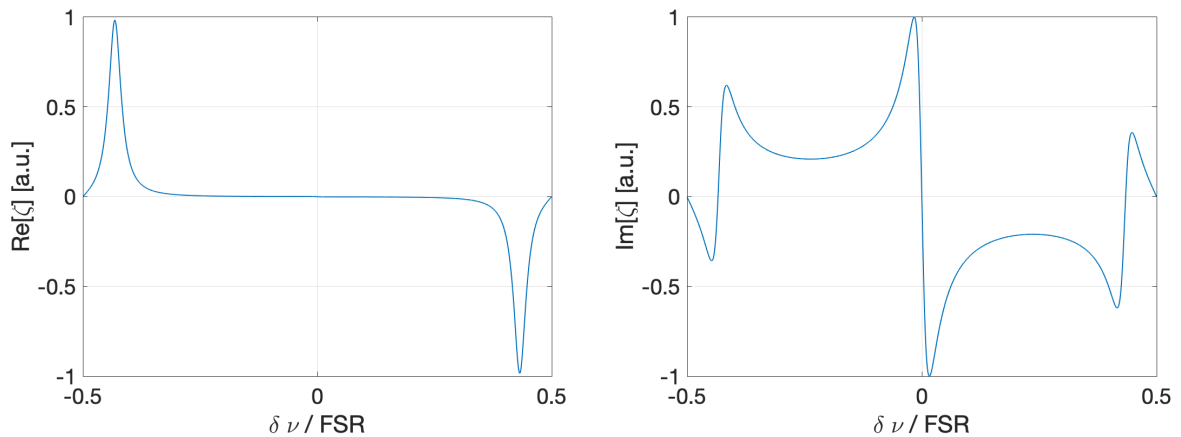


Figure 4.14: Normalised $\text{Re}[\zeta]$ (left) and normalised PDH error function ε (right) as a function of the normalised frequency $\delta\nu/\text{FSR}$ for a ring cavity with $\Omega_{\text{PDH}}/2\pi = 58\%$ of the FSR.

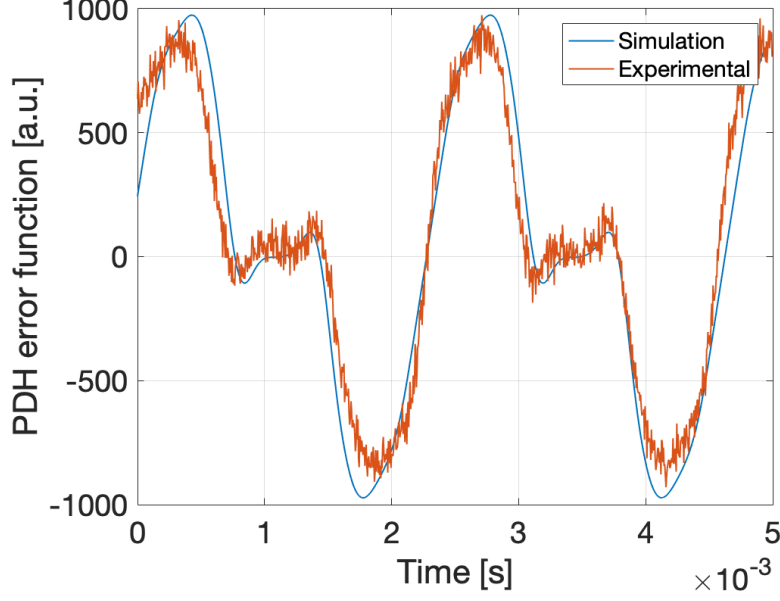


Figure 4.15: PDH error signal ε as a function of the time [s] for the reservoir cavity during a sweep of the Digilock. PDH Modulation amplitude $V_{\text{PDH}} = 0.4 V_{\text{PP}}$ (peak to peak), PDH modulation frequency $\nu_{\text{PDH}} = 3.13$ MHz, intra-cavity modulation depth $m = 2$, intra-cavity modulation frequency $\nu_{\text{mod}} = 19.9998$ GHz. The theoretical curve has been rescaled in order to be compared with the experimental curve.

4.4.3 Pound-Drever-Hall technique for the reservoir

The PDH technique can be applied to stabilise the reservoir, but error needs to be slightly modified to take into account the presence of different wavelengths inside the cavity. The result is actually quite straightforward if one recalls the results from section 4.3.1. The reflected field is simply given by $\mathbf{E}_{\text{ref}} = E_0 \sum_{n=-\eta}^{\eta} R_{n,0}(\omega) \hat{\mathbf{e}}_n$ thanks to the reservoir transfer matrix \mathbf{R} given by equation (4.20) and that the PD cannot capture beatings whose frequencies are integer multiples of 20 GHz. With these two elements in mind, $\zeta(\omega)$ becomes:

$$\zeta(\omega) = \sum_{n=-\eta}^{\eta} R_{n,0}(\omega) R_{n,0}^*(\omega + \Omega_{\text{PDH}}) - R_{n,0}^*(\omega) R_{n,0}(\omega - \Omega_{\text{PDH}}) \quad (4.42)$$

The error function ε remains defined as the imaginary part of ζ . In figure 4.15, one can observe that the theoretical model is in line with the measured error function. Just like the reflectivity of the reservoir \mathcal{R} , the shape of the PDH error function depends on the intra-cavity modulation frequency. The graph does not have the same shape as the one from figure 4.14, but since it exhibits regions with steep slopes, it can be used to stabilise the reservoir. In practice, the Digilock handles all the data-processing that has been introduced in this section, and the PID regulation as well.

4.5 Characterisation of the stabilisation performance for different regimes

This section presents the performances that can be achieved when stabilising the reservoir with the help of the PDH scheme, which is the core issue tackled in this thesis.

First, the problem is recalled and specified in a comprehensive way, then the experimental procedure followed to obtain relevant data is presented, and finally the actual results are shown and discussed.

As already claimed, the PDH technique is capable of stabilising the cavity at any phase, provided that the slope of the PDH error function is steep enough for this phase. Therefore, one of the features being investigated experimentally is the determination of the range of phases at which the cavity can be stabilised. This is of great practical importance, because as shown in section 3.9, the phase accumulated at each round trip is a global parameter that can alter the performances of the RC.

Another element that has been studied experimentally is the quality of the stabilisation. First, one has to use a relevant metric to assess how good the reservoir is stabilised. What is used throughout this section is the standard deviation of the phase during one run of measurements. Assume one is stabilising the reservoir at phase ϕ for some time. The phase inevitably fluctuates, but the better the cavity is stabilised, the lower these fluctuations. By recording the change of the phase, one can compute the standard deviation, the so-called phase noise, which therefore gives a quantitative indication on the efficiency of the stabilisation. This estimation can be done based on different kinds of signals, as it is explained in section 4.5.1.

The PDH technique also has its drawbacks. The phase modulation required to break the symmetry exhibited by the transfer function of the reservoir induces oscillations in the incident electric field, and therefore on the reflected power. The amplitude of these oscillations is mostly dependent on the PDH modulation amplitude and can be detrimental to the performances of the RC. Intuitively, one can understand that if A_{PDH} is increased, this will result in larger oscillations, which is problematic because in general, boosting the modulation amplitude allows to obtain a sharper PDH error function, with a better SNR, ultimately enabling to reach a more robust stabilisation. A trade-off has to be found between a high-performance stabilisation scheme and low PDH phase modulation amplitude, as one does not want to improve one feature at the cost of completely deteriorating the other.

These different issues are investigated for different PDH phase modulation regimes, namely couple of values of A_{PDH} and Ω_{PDH} . At the end of the day, this thorough characterisation of the stabilisation properties of the reservoir allows one to choose the regulation parameters that lead to the best chance of making the RC work.

4.5.1 Approach

Before explaining the experimental procedure, a few points have to be discussed. First, compared to an actual RC experiment, the characterisation procedure is simplified because the amplitude of the electric field is not modulated by the MZM. As a reminder, during an RC experiment, the light source driving the cavity has to be modulated in intensity to carry the data to be processed. In practice, the intensity modulation deteriorates the stabilisation signals, and this will need to be taken into account in the future, yet it has been neglected in the present analysis because not all challenges can be tackled at the same time. What is assumed, however, is that the PDH regime allowing to reach the best stabilisation is the same regardless of the intensity modulation being active or not.

To avoid any confusion, let us introduce the terminology used in this section:

- Transfer function: this is the transfer function of the cavity \mathcal{R} (time-independent)

- Reflected power: this is the power reflected by the reservoir (time-dependent)
- Error function: this is the PDH error function of the cavity ε (time-independent)
- Error signal: this is the instantaneous PDH error (time-dependent)

As far as the experimental parameters are concerned, preliminary numerical simulations² showed that RC tends to exhibit better performances when ν_{mod} is close to, but not exactly, an integer number of times the FSR. Therefore, the intra-cavity modulation was chosen with $\nu_{\text{mod}} = 19.9998$ GHz, and with a modulation power $P_{\text{mod}} = 20$ dBm ($m = 2$). This modulation frequency is obtained by taking the one at which the first sideband is at resonance detuned by 500 kHz. It is therefore important to note that all the results of this section will only be valid for this modulation frequency, since changing it completely modifies the transfer and error functions of the reservoir. The characterisation covers different PDH regimes: the modulation frequency ν_{PDH} take the values 390 kHz, 781 kHz, 1.56 MHz and 3.13 MHz and the modulation amplitude V_{PDH} 0.2 V_{PP} , 0.3 V_{PP} and 0.4 V_{PP} . For all the frequencies, the three voltages are investigated except for $\nu_{\text{PDH}} = 390$ kHz where only $V_{\text{PDH}} = 0.4 V_{\text{PP}}$ is studied. A peculiarity of the regulation for the reservoir is that the proportional and derivative terms of the PID have no influence on the stabilisation. At this point, there is no clear explanation on why it is the case, but performing a proper characterisation of the step responses of all the devices involved in the regulation could bring some insight. Furthermore, the impact of the value of k_I , the integral coefficient on the PID, on the stabilisation is very limited. Several order of magnitude can be spanned without altering significantly the quality of the regulation. The coefficient was set heuristically to $k_I = 17\,000$ V s⁻¹ because around this value the results seemed better, and was kept constant for all the measurements.

In the following paragraphs, the different quantities experimentally studied are presented, and the methodology followed to compute is explained.

Phase

The first key feature to determine is the phase at which one is stabilising. In practice, to choose the stabilisation position, a PDH error signal level is selected as reference using the Digilock. To relate the PDH error signal value to a phase, one needs to use both the error signal and the transfer function, as depicted in figure 4.16. The transfer function is used to determine the position of the anti-resonance, located at the maxima, which corresponds to a phase of $\pm\pi/2$ rad. Let $A \equiv (t^*, \varepsilon^*)$ be the point whose y -coordinate corresponds to the reference error function value ε^* set up in the Digilock. If T is the delay between two maxima of the transfer function, and if Δt is the time interval between t^* and the first maximum, then the phase is given by:

$$\phi = -\frac{\pi}{2} + \frac{\Delta t}{T}\pi \quad (4.43)$$

Let the region of the PDH error function comprised between the two maxima of the transfer function be the restricted error function. For a given PDH error function value ε^* , if there exists several points $B \equiv (t, \varepsilon^*)$ in the restricted region, then it might be possible to stabilise at this value ε^* , but it will be impossible to infer the corresponding phase.

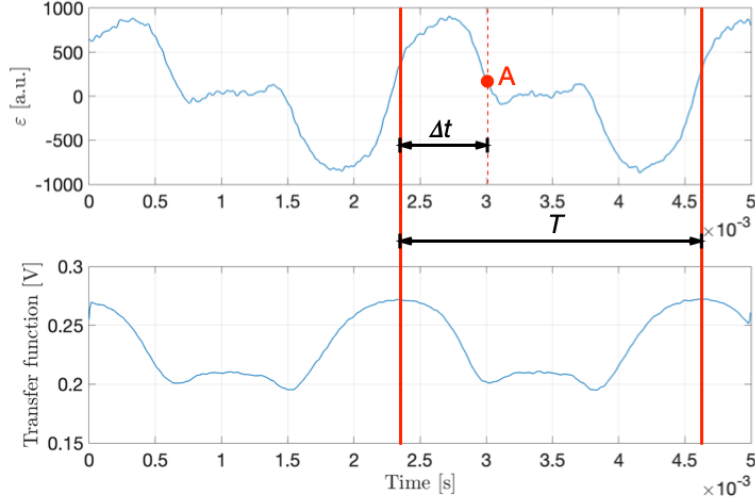


Figure 4.16: Error function [a.u.] and transfer function [V] as a function of the time [s] with $A_{\text{PDH}} = 0.4 V_{\text{PP}}$ and $\nu_{\text{PDH}} = 3.13 \text{ MHz}$, and schematic representation of the method followed to compute the phase. The point A is the point at which the reservoir is stabilised. T is the time taken during a sweep to go over two anti-resonances. Δt is the delay separating the x -coordinate of A from the first anti-resonance.

Pound-Drever-Hall signal

The next value of interest is the phase noise estimated based on the error signal. On the figure 4.18, one can see the evolution of the PDH error signal when the reservoir is being stabilised at -300 a.u. . Based on these data, one can easily compute the standard deviation of the error signal $\sigma(\varepsilon^*)$. This value still needs to be translated into a phase noise. To do so, one uses the error function displayed on the figure 4.17. First, one linearises the error function at the point of interest, which is represented by the red line segment on the figure. This allows to locally link $\sigma(\varepsilon^*)$ to a time variation Δt . Because the relation linking the wavelength of the laser to the piezo voltage is proportional, the ratio between Δt and T (the delay between two maxima, as previously) is the same as the ratio between σ_{PDH} , the phase noise in rad, and π . If one defines α as the slope of the tangent at the point of interest (in a.u. s^{-1}), the phase noise reads:

$$\sigma_{\text{PDH}} = \frac{\sigma(\varepsilon^*)_{\text{PDH}}}{|\alpha|T} \pi \quad (4.44)$$

This justify why it is better to work with steep slopes when using the PDH technique.

Reflected power

The method to obtain the phase noise based on the reflected power is similar to that of the PDH error signal. The only difference is that it requires one more step, due to the fact that this time, the slope of the transfer function is needed instead of that of the error signal. In figures 4.19 and 4.21, one can see that, as mentioned in the introduction, the PDH phase modulation introduces oscillations. This implies that this transfer function cannot be used directly because linearising such an oscillating curve does not make much sense. Another solution has to be explored. The idea is to use a transfer function measured without PDH phase modulation, as the one displayed in figure 4.20. Let $A \equiv (\Delta t_1, \varepsilon^*)$

²Courtesy to Lorenz Butschek

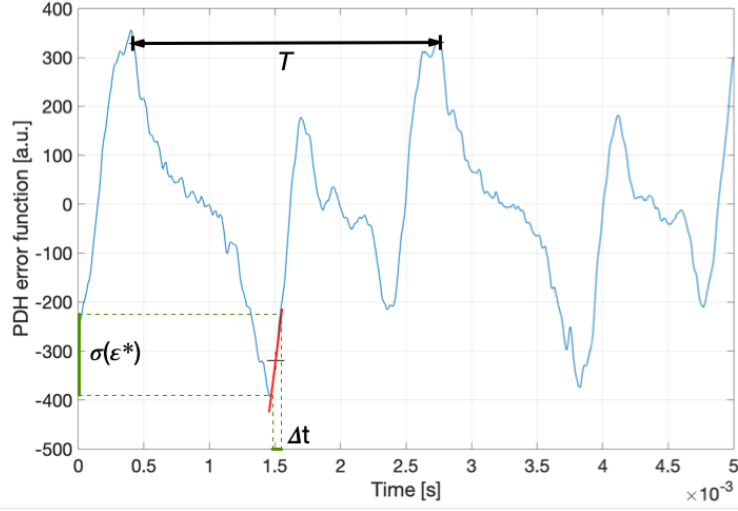


Figure 4.17: Error function as a function of the time [s] with $A_{\text{PDH}} = 0.4 V_{\text{PP}}$ and $\nu_{\text{PDH}} = 390 \text{ kHz}$, reservoir stabilised at $\varepsilon^* = -300 \text{ a.u.}$ Error signal for this stabilisation is represented in figure 4.18.

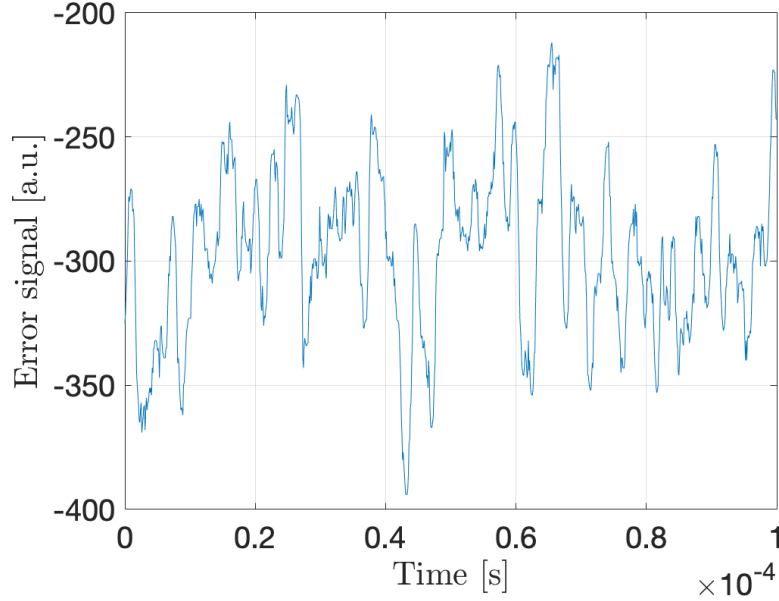


Figure 4.18: Error signal as a function of the time [s] with $A_{\text{PDH}} = 0.4 V_{\text{PP}}$ and $\nu_{\text{PDH}} = 390 \text{ kHz}$, reservoir stabilised at $\varepsilon^* = -300 \text{ a.u.}$ The experimental conditions are the same as in 4.17.

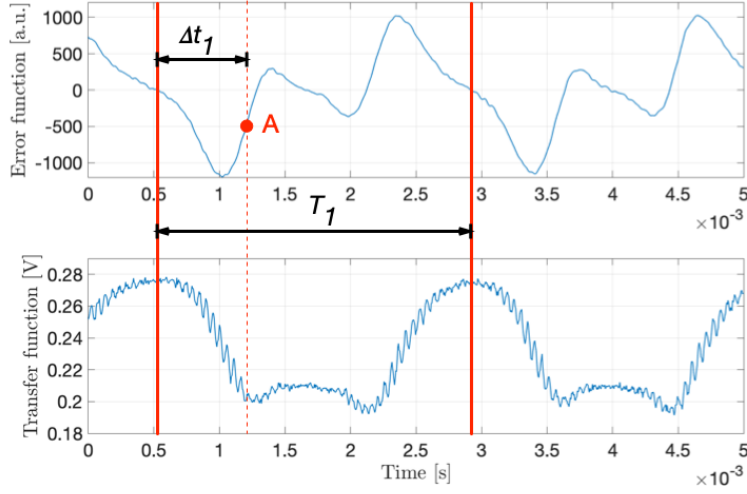


Figure 4.19: Error function and transfer function [V] as a function of the time [s], with $A_{\text{PDH}} = 0.4 \text{ V}_{\text{PP}}$ and $\nu_{\text{PDH}} = 781 \text{ kHz}$, and with the reservoir stabilised at $\varepsilon^* = -500 \text{ a.u.}$. The reflected power for this stabilisation is illustrated in figure 4.21.

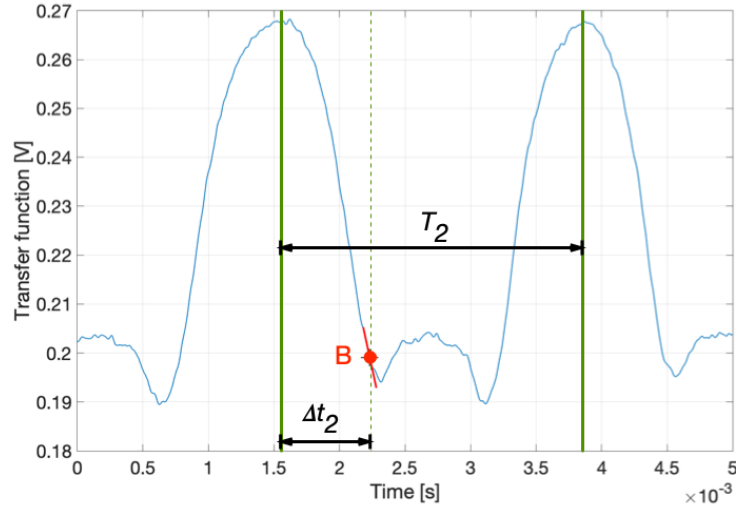


Figure 4.20: Transfer function [V] as a function of the time [s] without PDH modulation, with the reservoir stabilised at $\varepsilon^* = -500 \text{ a.u.}$. It is the same transfer function as in figure 4.19, except that there is no phase modulation to be able to compute the slope at the point B . The point B corresponds to the same stabilisation position than the point A in figure 4.19. The x -coordinate of B reads $\Delta t_2 = \frac{\Delta t_1}{T_1} T_2$. The reflected power for this stabilisation is illustrated in figure 4.21.

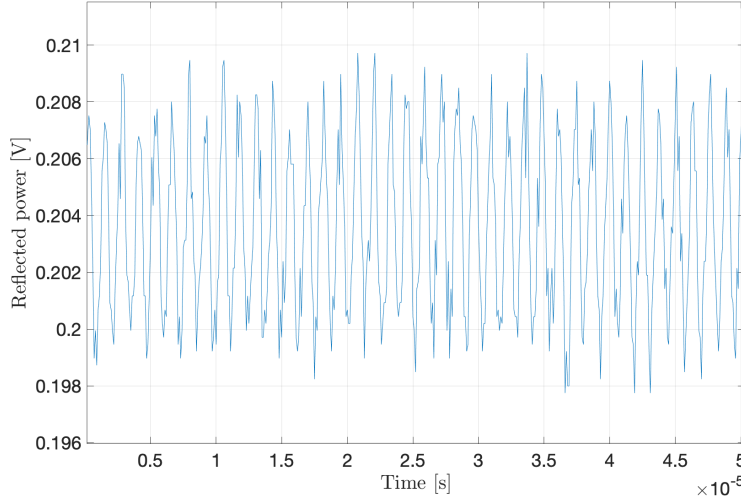


Figure 4.21: Reflected power [V] as a function of the time [s] with $A_{\text{PDH}} = 0.4 V_{\text{PP}}$ and $\nu_{\text{PDH}} = 781 \text{ kHz}$ and with the reservoir stabilised at $\varepsilon^* = -500 \text{ a.u.}$. The experimental conditions are the same as in figures 4.19 and 4.20.

be the point at which the cavity is stabilised whose phase can be determined using the method presented above. Its x -coordinate can be reduced assuming that one is working in the restricted region. One would like to determine the point $B \equiv (\Delta t_2, V^*)$ on the figure 4.20 that has the same phase as A . If T denotes the delay between two maxima and if the indices 1,2 represent the transfer function and without phase modulation respectively, then Δt_2 simply reads:

$$\Delta t_2 = \frac{\Delta t_1}{T_1} T_2 \quad (4.45)$$

Once the coordinates of the point B are known, the principle is identical to that of the previous one: measure the slope α_2 of the transfer function at point B (in V s^{-1}), use the data from figure 4.21 to calculate the standard deviation $\sigma(\varepsilon^*)_{\text{ref}}$ (in V) and compute the phase noise σ_{ref} (in rad) as:

$$\sigma_{\text{ref}} = \frac{\sigma(\varepsilon^*)_{\text{ref}}}{|\alpha_2| T_2} \pi \quad (4.46)$$

Phase noise amplitude

The phase fluctuations in the reflected power have two components, the PDH phase modulation and the actual phase noise. In this paragraph, the method used to estimate the former is presented. The basic idea is to perform a least square fit, as presented in section 4.3.2, but this time using a sinusoidal function defined as:

$$\mathcal{V}_{\text{ref}}(t; \mathcal{A}, \theta, \mathcal{A}_0) = \mathcal{A} \sin(\Omega_{\text{PDH}} t + \theta) + \mathcal{A}_0 \quad (4.47)$$

with \mathcal{A} , θ and \mathcal{A}_0 being the three parameters to be determined by the minimisation. Their value is given by:

$$(\mathcal{A}, \theta, \mathcal{A}_0) = \underset{(\mathcal{A}^*, \theta^*, \mathcal{A}_0^*)}{\text{argmin}} \sum_{i=0}^T (V_{\text{ref},i} - \mathcal{V}_{\text{ref}}(t_i; \mathcal{A}^*, \theta^*, \mathcal{A}_0^*))^2 \quad (4.48)$$

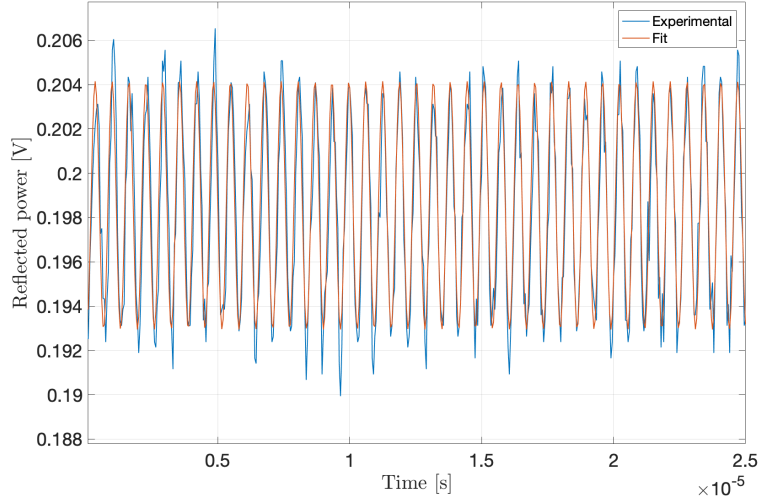


Figure 4.22: Reflected power [V] as a function of the time [s] with $A_{\text{PDH}} = 0.3 V_{\text{PP}}$ and $\nu_{\text{PDH}} = 1.56 \text{ MHz}$ and with the reservoir stabilised at $\varepsilon^* = 300 \text{ a.u.}$. Experimental data and sinusoidal fit. The corresponding residual reflected power is illustrated in figure 4.23.

With T the total number of data points, $V_{\text{ref},i}$ the value of the reflected power and t_i the time of the i^{th} sample. In figure 4.22, the result of the optimisation is shown with the experimental data represented in blue, and the sinusoidal fitting in orange. It is now assumed that \mathcal{V}_{ref} is the part of the reflected power that is due to the phase modulation. The formula to compute the phase noise based on the transfer function derived in the previous paragraph can be adapted to this situation by considering that the spreading of the signal is due to the oscillation amplitude \mathcal{A} (in V). The phase modulation amplitude $\Delta\varphi$ (in rad) is given by:

$$\Delta\varphi = \frac{\mathcal{A}}{|\alpha_2|T_2}\pi \quad (4.49)$$

This computation relies on measures extrapolated from the reflected power and not from the error signal, hence the use of the α_2 and T_2 in this new formula.

The phase modulation amplitude can be detrimental to the performance of the RC because it will add noise on the input. Ironically, the phase modulation amplitude that is observed because of the fact that the PDH technique is required to stabilise the reservoir could prevent it from working as a RC. This explains why both the phase noise and the phase modulation amplitude need to be minimised.

Residual reflected power

What is called the residual reflected power is the part of the fluctuations of the reflected power that is not due to the oscillations. It is defined as:

$$V_{\text{res}}(t) = V_{\text{ref}}(t) - \mathcal{V}_{\text{ref}}(t) \quad (4.50)$$

The residual power coming from the signals depicted on the figure 4.22 is shown in figure 4.23. Once again, the previous formula can be used, provided that one uses $\sigma(\varepsilon^*)_{\text{res}}$ (in V) instead of $\sigma(\varepsilon^*)_{\text{ref}}$ to determine the phase noise based on the residual power σ_{res} (in rad):

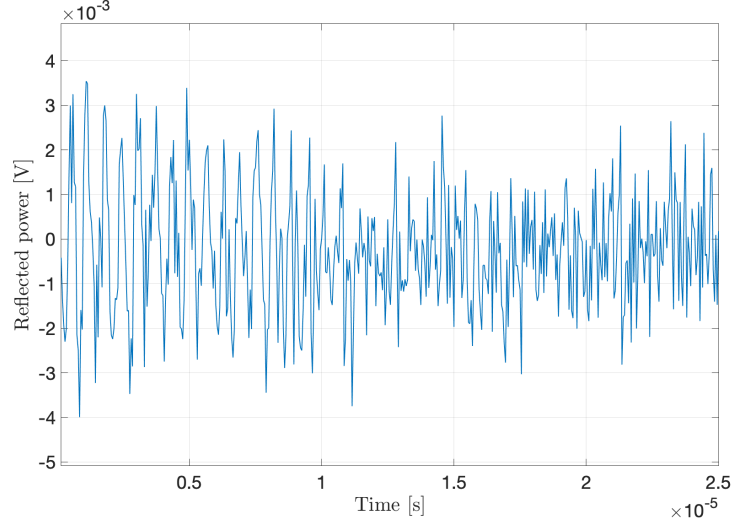


Figure 4.23: Residual reflected power [V] as a function of the time [s] with $A_{\text{PDH}} = 0.3 \text{ V}_{\text{PP}}$ and $\nu_{\text{PDH}} = 1.56 \text{ MHz}$ and with the reservoir stabilised at $\varepsilon^* = 300 \text{ a.u.}$

$$\sigma_{\text{res}} = \frac{\sigma(\varepsilon^*)_{\text{res}}}{|\alpha_2|T_2}\pi \quad (4.51)$$

Long time-scale Pound-Drever-Hall signal

To be able to distinguish the modulation oscillations, the sampling frequency of the Digilock has to be at least twice the maximum PDH modulation frequency, which is 3.13 MHz, as required by the Shannon-Nyquist sampling theorem. To achieve higher sampling frequencies, the Digilock has to record data sets over shorter time-scales, as low as a few tens of microseconds, as can be seen on the time axis of the figure 4.23, for example. The problem is that the duration of a RC experiment is in the order of the ms. The long time-scale PDH phase noise is simply a generalisation of the PDH phase noise, but measured on a longer time-scale (5 ms), to ensure the robustness of the stabilisation scheme over the long run. Let $\sigma(\varepsilon^*)_{\text{PDH,l}}$ be the standard deviation of the PDH error signal recorded over 5 ms (in a.u.). The long time-scale PDH phase noise $\sigma_{\text{PDH,l}}$ (in rad) is computed in exactly the same way as the PDH phase noise, except that $\sigma(\varepsilon^*)_{\text{PDH,l}}$ is used instead of $\sigma(\varepsilon^*)_{\text{PDH}}$:

$$\sigma_{\text{PDH,l}} = \frac{\sigma(\varepsilon^*)_{\text{PDH,l}}}{|\alpha|T}\pi \quad (4.52)$$

4.5.2 Results

The results of the measurements can be found in the tables of the appendix A. For each PDH configuration and for each PDH stabilisation position ε^* , five data sets were measured in order to obtain results that are statistically more significant. In the tables, ϕ , σ_{PDH} , $\sigma_{\text{PDH,l}}$, σ_{ref} , $\Delta\varphi$ and σ_{res} are averages taken over the data sets, and $\mathcal{S}(\dots)$ are their respective standard deviations. The dimension of the different values is in mrad unless specified otherwise.

At the bottom of the tables, there is an additional row. It corresponds to the values obtained at a position indicated by ε^* , but with a value of k_I decreased to only 500 V s^{-1} .

This is done in anticipation of actual RC experiments for which this parameter needs to be smaller. During a run of the RC, the input power of the reservoir is modulated in intensity, therefore a change of the reflected power can be due to a variation of the input power, and not necessarily to a phase fluctuation. Decreasing the integral coefficient of the PID makes it less likely to overreact to an intensity modulation. For each configuration, the stabilisation performance are only computed at one position, because this is done only to have a first idea of how a smaller k_I impacts the reservoir.

For some ε^* , there is an additional value called the *challenger*, which is a heuristic used to determine the best stabilisation configuration and position. It is defined as the product:

$$\text{Challenger} = \sigma_{\text{PDH}} \cdot \Delta\varphi \quad (4.53)$$

Recalling that both σ_{PDH} and $\Delta\varphi$ should be as small as possible, the best configuration is the one minimising the challenger. Note that there might exist more sophisticated heuristics leading to better results, but the challenger was used as a first approach thanks to its simplicity. The challenger was only computed for stabilisation positions for which the confidence in the measurements is the highest, and that are supposed to be usable in a practical RC experiment. This condition excludes the positions:

- For which a given value of ε^* can correspond to different phases.
- At which the slope of the transfer function is close to zero, which means that one is close to a minimum. This implies that linearising the transfer function at this point is not very relevant because this approximation rapidly becomes invalid, and that the phase noises deduced from this operation can be inaccurate.
- Where σ_{PDH} , $\sigma_{\text{PDH},l}$ and σ_{res} are not included in an interval 10 mrad wide, all at the same time. When they are included, it increases the confidence in the measurements because it suggests that similar phase noises can be obtained in three different ways.

The five configurations and positions most likely to meet the criteria are presented in table 4.1. A striking feature emerging from these results is the fact the PDH modulation frequency is the same for all the candidates. Therefore, when setting up a RC experiment, one should pay attention to use a PDH modulation frequency of 781 kHz.

Rank	A_{PDH} [V _{PP}]	ν_{PDH} [kHz]	ε^* [a.u.]	ϕ [rad]	Challenger [mrad ²]
#1	0.4	781	400	1.3	1166
#2	0.2	781	-300	-1.43	1308
#3	0.4	781	700	1.45	1349
#4	0.3	781	500	1.31	1449
#5	0.4	781	600	1.39	1506

Table 4.1: Top-5 ranking of the positions and configurations

One important remark concerns the phase modulation amplitudes. In theory, for a given configuration, they should be constant, since A_{PDH} is not changed. When looking at the data in appendix A, one notices that it is not the case, even when restricting the list of results to those with a challenger value (because one has more confidence on the quality of their measure). At this point, there is no satisfying explanation on why the modulation amplitude experiences position-dependent fluctuations. This incoherence can

come from two main sources: the raw data measurement and the software post-processing. Regarding the former, most of the time during the measurements an external oscilloscope was plotting the different signals, and their shape agreed with the signals of the Digilock. This does not mean that an error on the measurements is impossible, but this increases the confidence that can be placed in them. Regarding the software used to analyse the results, there are two main components: the least square fitting of the sine function, and the slope estimator. The first is a function used as a black box leading to satisfying results, with a 95 % confidence interval on the oscillation amplitude \mathcal{A} very narrow (less than a percent relative to \mathcal{A}). This suggests that the failing component of the code is the estimation of the slope of the transfer function, even though the algorithm was always supervised while running, and did not seem to return aberrant results. One thing is certain, in the future, this phase modulation issue should be further investigated. This would benefit the whole experiment by making the characterisation results more solid.

Chapter 5

Conclusion

In this master thesis, the experimental study of an interferometric stabilisation of a WDM PRC has been tackled. First, the notion of RC has been discussed. The RC computation paradigm is based on the concept of RNN. It reaches state of the art performances in tasks involving the processing time-dependent inputs. It was shown that the neurons inside the RC need to be connected in a random way, and that when being trained, a RC only requires its output weights to be updated unlike classical NNs. The mathematical model governing the discrete time evolution of a RC is very general and imposes very few conditions. This property allows to use physical systems other than classical silicon-based computers to implement the computing logic of a RC. This has already been done several times using optical setups with the different neurons being multiplexed in time and encoded in either the light intensity or in the electric field.

In the second part of this work, a new kind of photonic RC based on the WDM of the neurons has been introduced. The main advantage of this scheme is that all the neurons are updated in the same time, enabling an increase of the processing speed. This new optical RC is implemented using a fibre-based setup, with the RC computing logic taking place inside a ring cavity and with the mixing of the neurons being performed by a PM. In this scheme, the input signal is encoded in the amplitude of the electric field emitted by a laser source. At the exit of the ring cavity, the signal is demultiplexed and the output of the RC is computed by linearly combining the intensity of the different frequency components of the electric field encoding the neurons. Because of practical limitations to which the PM is subject, only a limited number of neurons can coexist in the optical cavity at the same time, which is a drawback of this scheme.

The last chapter of this thesis has been dedicated to the experimental study of the interferometric stabilisation properties of the optical cavity called the reservoir. It has been shown that the reservoir behaves like an interferometer and that interesting properties about the phase of the electric field inside it can be deduced by studying the power it reflects. This phase, which is the one acquired by the electric field during one round trip around the cavity, is an important parameter of the reservoir and one should be able to maintain it constant during a RC experiment, this is why the stabilisation of this cavity is such an important issue. The experimental setup has been presented and three main parts emerged from this description: a first block handles the shaping of the input electric field, with notably a narrow band laser and a MZM, a second one includes the reservoir cavity and the readout of the neurons, and a last one takes care of stabilising the cavity. Different features of the reservoir not directly linked to its stabilisation have been characterised. First an analytical model of the transfer function of the reservoir, which is

essentially the reflected power as a function of the phase, has been derived and validated with the help of experimental curves. After that, the effective losses experienced by an electric field inside the cavity were estimated, and finally, the influence of the modulation power on the modulation depth and by extension on the transfer function was studied. The PDH cavity stabilisation technique has been presented. This powerful tool allows to build more robust stabilisation scheme because it is able to extract more information about the phase of the electric field than the classical transfer function. By using an additional PM and some electronic post-processing, a more sophisticated transfer function called the error function is constructed and serves as a basis for higher quality regulations. The core of this chapter was the comparison between the different stabilisation strategies. To do so, a quantitative indicator, the phase noise, has been extensively used and was computed for each strategy and set point with different methods. The key take-away of this analysis is that the best results were always obtained with a PDH phase modulation frequency of 781 kHz. For future RC experiments, I would suggest to use this modulation frequency.

An actual RC experiment was attempted using the values provided by the analysis presented in this thesis to get some preliminary results. Unfortunately, it was not possible to get the reservoir to work since the noise was still too important. The decrease of the integral parameter of the PID parameter is probably not to blame, because as can be seen on the tables of appendix A, the phase noises in the last rows are not dramatically larger. One possible explanation is that the stabilisation scheme cannot handle the intensity modulation, which would make sense since it has not been designed with this constraint in mind. This gives perspectives for a future work in which the characterisation performed in this thesis would be made more relevant by including the influence of the input intensity modulation on the stabilisation performances. Also, the erratic behaviour of the phase modulation amplitude should be further investigated in order to find its origin.

Appendix A

Experimental results

57

ε^* [a.u.]	ϕ [rad]	σ_{PDH}	$\mathcal{S}(\sigma_{\text{PDH}})$	$\sigma_{\text{PDH},1}$	$\mathcal{S}(\sigma_{\text{PDH},1})$	σ_{ref}	$\mathcal{S}(\sigma_{\text{ref}})$	$\Delta\varphi$	$\mathcal{S}(\Delta\varphi)$	σ_{res}	$\mathcal{S}(\sigma_{\text{res}})$	Challenger [mrad ²]
-300	-0.8	44.08	4.56	44.78	1.11	72.05	3.55	86.93	3.09	37.5	3.37	3661
-200	-0.75	36.22	4.56	38.73	0.75	49.42	1.31	56.85	1.31	28.71	1.09	1964
-100	-0.7	22.53	3.68	22.97	0.81	59.07	1.69	56.89	1.94	43.23	1.2	
-100	0.44	27.26	4.45	27.8	0.98	47.9	1.37	46.13	1.57	35.05	0.97	
100	-0.66	56.69	12.72	57.4	1.86	85.39	4.09	81.11	3.74	63.18	4.35	
100	0.54	20.86	4.44	20.06	0.65	85.14	4.08	80.87	3.73	63	4.34	
200	0.59	35.49	4.88	38.56	1.46	88.79	2.1	102.11	2.2	51.59	2.42	
-200	-0.75			67.66	19.3	66.43	12.8					

Table A.1: Experimental results for PDH modulation amplitude $A_{\text{PDH}} = 0.4 \text{ V}_{\text{PP}}$, PDH modulation frequency $\nu_{\text{PDH}} = 390 \text{ kHz}$

ε^* [a.u.]	ϕ [rad]	σ_{PDH}	$\mathcal{S}(\sigma_{\text{PDH}})$	$\sigma_{\text{PDH,l}}$	$\mathcal{S}(\sigma_{\text{PDH,l}})$	σ_{ref}	$\mathcal{S}(\sigma_{\text{ref}})$	$\Delta\varphi$	$\mathcal{S}(\Delta\varphi)$	σ_{res}	$\mathcal{S}(\sigma_{\text{res}})$	Challenger [mrad ²]
-500	-0.81	30.07	2.83	29.82	0.68	58.73	0.64	75.29	0.67	24.76	0.97	2124
-400	-0.76	50.21	4.58	51.12	0.75	53.83	0.71	66.02	1.45	26.71	1.37	
-300	-0.71	25.2	1.44	24.99	0.6	44.67	0.88	51.87	1.22	25.48	0.81	1308
-200	-0.68	23.8	1.4	23.37	0.38	139.88	2.73	143.53	6.36	96.11	2.94	
-100	-0.64	22.43	1.64	23.09	0.57	62.09	0.76	55.99	2.06	47.79	0.94	
-100	0.41	42.68	3.12	43.94	1.09	39.38	0.48	35.51	1.31	30.31	0.6	
100	-0.51	57.88	3.03	54.36	0.64	56.26	1.15	46.1	1.2	45.83	1.65	
100	0.53	22.15	1.16	20.81	0.24	123.14	2.51	100.89	2.63	100.31	3.62	
200	0.57	38.81	2.83	39.37	1.23	58.41	0.93	59.52	0.97	40.47	1.05	2354
300	0.61	22.82	1.51	23.44	0.57	79.75	2.13	93.18	2.81	44.88	1.07	
400	0.67	35.87	2.68	35.24	1.08	54.09	0.5	66.72	0.72	26.41	0.81	2169
-300	-0.71			46.75	13.1	69.36	17.87					

Table A.2: Experimental results for PDH modulation amplitude $A_{\text{PDH}} = 0.2 V_{\text{PP}}$, PDH modulation frequency $\nu_{\text{PDH}} = 781 \text{ kHz}$

ε^* [a.u.]	ϕ [rad]	σ_{PDH}	$\mathcal{S}(\sigma_{\text{PDH}})$	$\sigma_{\text{PDH,l}}$	$\mathcal{S}(\sigma_{\text{PDH,l}})$	σ_{ref}	$\mathcal{S}(\sigma_{\text{ref}})$	$\Delta\varphi$	$\mathcal{S}(\Delta\varphi)$	σ_{res}	$\mathcal{S}(\sigma_{\text{res}})$	Challenger [mrad ²]
-700	-0.8	19.12	0.98	19.5	0.64	120.59	1.08	162.04	1.44	37.39	0.72	
-600	-0.77	17.16	0.73	17.55	0.34	82.78	1.07	109.33	1.21	29.48	1.03	
-500	-0.74	18.38	1.2	19.2	0.37	74.65	0.9	96.24	1.1	30.58	1.4	
-400	-0.72	16.56	1.07	16.25	0.34	58.53	1.06	73.56	1.4	26.77	0.63	
-300	-0.7	15.19	1.58	15.57	0.47	56.03	1.39	66.85	2.14	30.04	0.29	
-200	-0.69	15.06	1.44	14.3	0.32	151.58	3.48	167.17	3.88	94.82	2.49	
-200	0.41	30.73	2.94	29.18	0.65	50.55	1.16	55.75	1.29	31.62	0.83	
-100	-0.66	14.29	1.23	14.37	0.18	82.11	1.4	83.89	2.25	56.73	1.36	
-100	0.47	31.58	2.72	31.76	0.39	226.27	3.86	231.18	6.21	156.32	3.76	
100	-0.59	23.69	1.79	24.66	0.36	87.12	1.58	88.71	2.3	60.42	0.77	
100	0.54	20.96	1.58	21.83	0.32	87.05	1.58	88.64	2.3	60.37	0.77	
200	0.57	19.99	1.72	20.4	0.56	63.5	0.77	69.63	1.31	40.07	0.78	
300	0.59	15.89	1.63	15.66	0.55	86.2	1.09	102.7	2.59	46.35	1.33	
400	0.62	21.7	2.62	21.98	0.62	79.12	0.67	99.28	1.31	36.41	1.33	
500	0.65	20.58	1.45	19.31	0.46	54.31	0.62	70.15	0.9	22.07	0.49	1449
600	0.67	19.2	1.21	19.59	0.57	76.25	0.65	100.99	1.13	26.91	0.8	2212
-300	-0.7			29.85	7.4	64.93	7.02					

Table A.3: Experimental results for PDH modulation amplitude $A_{\text{PDH}} = 0.3 \text{ V}_{\text{PP}}$, PDH modulation frequency $\nu_{\text{PDH}} = 781 \text{ kHz}$

ε^* [a.u.]	ϕ [rad]	σ_{PDH}	$\mathcal{S}(\sigma_{\text{PDH}})$	$\sigma_{\text{PDH,l}}$	$\mathcal{S}(\sigma_{\text{PDH,l}})$	σ_{ref}	$\mathcal{S}(\sigma_{\text{ref}})$	$\Delta\varphi$	$\mathcal{S}(\Delta\varphi)$	σ_{res}	$\mathcal{S}(\sigma_{\text{res}})$	Challenger [mrad ²]
-1000	-0.85	27.64	1.15	30	0.39	86.27	0.89	118.52	1.26	20.26	1.41	3078
-900	-0.81	18.19	1.43	18.06	0.38	99.96	0.63	136.75	0.85	25.15	1.12	2799
-800	-0.79	13.68	1.51	14.26	0.23	148.32	1.62	201.66	1.63	40.53	2.26	
-700	-0.77	17.9	1.57	17.39	0.47	95.42	0.76	128.27	1.45	29.51	1.41	2771
-600	-0.74	22.7	1.51	23.68	0.45	88.02	0.26	117.12	0.51	29.65	1.25	2968
-500	-0.72	15.5	2.67	15.97	0.52	68.54	0.93	89.22	1.62	26.7	1.56	
-400	-0.69	14.74	1.99	13.94	0.2	96.58	0.96	122.41	2.06	42.73	1.32	
-300	-0.68	13.69	1.58	14.39	0.36	193.24	4.22	234.45	5.83	99.04	3.73	
-200	-0.65	16.4	0.58	18.1	0.49	81.43	1.06	94.16	0.84	46.81	1.32	
-200	0.49	20.92	0.73	23.09	0.62	811.36	10.55	938.23	8.38	466.49	13.14	
-100	-0.63	16.11	1.8	16.96	0.32	75.19	1.42	82.55	2.25	47.37	0.75	
-100	0.51	23.41	2.61	24.64	0.47	295.7	5.58	324.64	8.84	186.3	2.96	
100	-0.58	17.58	1.35	18.33	0.35	74	1.61	83.13	2.44	44.9	0.95	
100	0.58	17.06	1.31	17.79	0.34	64.79	1.41	72.79	2.13	39.31	0.83	
200	0.6	18.21	2.24	16.89	0.36	76.27	1.34	87.42	2.29	44.62	1.41	
300	0.63	15.76	1.37	15.17	0.37	63.15	0.93	75.55	1.93	33.59	1.03	
400	0.65	15.25	1.46	16.94	0.43	50.43	1.24	63.56	1.7	22.83	0.82	1166
500	0.67	20.11	1.62	19.45	0.49	65.75	0.8	85.45	1.37	25.84	0.82	1863
600	0.69	19.43	1.51	19.06	0.25	58.27	0.5	77.42	0.63	19.87	0.49	1506
700	0.72	17.96	0.89	19.75	0.35	55.31	0.32	74.6	0.52	16.55	0.66	1349
800	0.75	21.76	1.64	22.96	0.95	58.1	0.36	78.98	0.35	15.88	0.52	1595
-400	-0.69			37.98	9.55	110.43	6.02					

Table A.4: Experimental results for PDH modulation amplitude $A_{\text{PDH}} = 0.4 V_{\text{PP}}$, PDH modulation frequency $\nu_{\text{PDH}} = 781 \text{ kHz}$

ε^* [a.u.]	ϕ [rad]	σ_{PDH}	$\mathcal{S}(\sigma_{\text{PDH}})$	$\sigma_{\text{PDH,l}}$	$\mathcal{S}(\sigma_{\text{PDH,l}})$	σ_{ref}	$\mathcal{S}(\sigma_{\text{ref}})$	$\Delta\varphi$	$\mathcal{S}(\Delta\varphi)$	σ_{res}	$\mathcal{S}(\sigma_{\text{res}})$	Challenger [mrad ²]
-400	-0.96	82.81	2.17	83.66	1.65	61.38	0.86	81.48	1.18	21.08	0.63	2398
-300	-0.84	75.12	2.51	75.5	0.6	54.5	1.01	71.26	1.39	20.7	0.44	
-200	-0.78	31.03	1.21	31.78	0.59	62.77	1.41	80	2.35	27.13	0.29	
-100	-0.71	28.89	2.13	39.18	0.71	43.93	1.06	53.47	1.19	22.32	0.89	
100	0.41	58.03	5.66	56.7	1.52	51.63	0.9	62.55	1.48	26.58	0.52	
200	0.46	38.04	0.65	37.88	0.3	341.89	7.41	431.8	9	153.51	4.75	
300	0.52	66.03	5.52	63.4	0.97	281.99	4.72	369.3	6.85	106.09	1.31	
-200	-0.78			36.91	3	72.95	4.75					

Table A.5: Experimental results for PDH modulation amplitude $A_{\text{PDH}} = 0.2 V_{\text{PP}}$, PDH modulation frequency $\nu_{\text{PDH}} = 1.56 \text{ MHz}$

ε^* [a.u.]	ϕ [rad]	σ_{PDH}	$\mathcal{S}(\sigma_{\text{PDH}})$	$\sigma_{\text{PDH,l}}$	$\mathcal{S}(\sigma_{\text{PDH,l}})$	σ_{ref}	$\mathcal{S}(\sigma_{\text{ref}})$	$\Delta\varphi$	$\mathcal{S}(\Delta\varphi)$	σ_{res}	$\mathcal{S}(\sigma_{\text{res}})$	Challenger [mrad ²]
-500	-0.8	40.98	2.35	40.95	0.77	176.42	3.46	237.8	4.54	53.1	2.49	6936
-400	-0.72	45.42	3.83	47.46	1.35	118.11	2.35	158.27	3.32	37.59	0.74	
-300	-0.68	29.93	2.45	28.63	0.71	366.37	4.22	485.97	6.13	126.58	1.63	
-200	-0.65	46.57	3.07	45.99	1.08	158.49	1.79	206.94	2.45	60.7	1.14	
-100	-0.6	78.61	8.94	79.71	1.33	1486.13	9.35	1905.17	21.69	625.83	11.57	
100	-0.49	86.12	3.33	83.91	3.26	107.14	1.67	136.49	2.79	46.41	0.67	
100	0.52	49.25	1.9	47.98	1.86	2076.51	32.34	2645.29	54.07	899.52	13.01	
200	0.57	38.2	3.1	38.51	0.85	128.41	2.87	167.41	4.09	49.61	0.83	10857
300	0.61	55.16	2.82	56.14	1.47	149.91	0.87	198.17	2.05	53.06	1.76	
400	0.69	36.98	1.66	37.08	1.01	101.77	0.95	136.52	1.23	32.07	0.62	4830
500	0.72	163.53	12.6	177.98	2.9	82.01	1.34	110.51	1.97	24.76	0.66	
-300	-0.68			38.9	3.71	388.43	7.61					

Table A.6: Experimental results for PDH modulation amplitude $A_{\text{PDH}} = 0.3 V_{\text{PP}}$, PDH modulation frequency $\nu_{\text{PDH}} = 1.56 \text{ MHz}$

ε^* [a.u.]	ϕ [rad]	σ_{PDH}	$\mathcal{S}(\sigma_{\text{PDH}})$	$\sigma_{\text{PDH,l}}$	$\mathcal{S}(\sigma_{\text{PDH,l}})$	σ_{ref}	$\mathcal{S}(\sigma_{\text{ref}})$	$\Delta\varphi$	$\mathcal{S}(\Delta\varphi)$	σ_{res}	$\mathcal{S}(\sigma_{\text{res}})$	Challenger [mrad ²]
-800	-0.87	56.81	3.38	57.23	1.27	146.55	0.69	199.55	0.96	39.3	0.93	13518
-700	-0.8	46.18	2.82	46.64	0.6	202.34	1.29	275.47	2.01	54.4	1.08	
-600	-0.77	25.99	1.69	25.21	0.42	171.36	2.28	232.4	2.79	48.26	1.69	
-500	-0.73	48.03	2.19	47.11	0.5	149.37	1.95	201.31	2.54	44.12	1.1	9363
-400	-0.66	24.95	1.5	24.65	0.79	480.5	3.53	644.16	4.61	152.3	2.89	
-300	-0.67	39.26	3.71	39.63	0.47	535.94	7.95	713.98	13.87	178.9	8.88	
-200	-0.64	24.3	1.8	24.02	0.4	188.77	2.24	249.37	3.22	67.14	1.41	
-100	-0.6	79.43	3.88	78.96	2.52	359.78	2.99	473.63	3.18	130.94	5.62	
-100	0.35	33.14	1.62	32.95	1.05	103.46	0.86	136.2	0.92	37.65	1.62	
100	-0.52	62.38	6.29	62.1	2.17	192.32	1.46	251.94	2.02	72.25	1.21	
100	0.42	88.35	8.91	87.96	3.08	93.53	0.71	122.51	0.98	35.14	0.59	
200	0.47	37.52	2	41.91	1.35	3063.85	16.68	4048.26	18.91	1088.31	22.56	
300	0.51	23.5	1.96	23.25	0.53	407.62	4.32	542.7	7.18	136.82	4.82	
400	0.54	68.29	2.78	67.91	1.29	313.75	5.02	422.95	6.9	94.36	2.63	
500	0.58	41.94	0.9	40.04	0.54	256.52	1.32	347.05	1.49	74.3	1.39	
600	0.62	33.25	1.88	34.64	0.43	207.43	2.25	281.17	3.01	58.77	1.88	11549
700	0.68	53.34	6.04	56.33	1.63	165.25	0.96	225.04	1.32	44.29	0.4	
-400	-0.66			37.95	5.01	503.69	12.07					

Table A.7: Experimental results for PDH modulation amplitude $A_{\text{PDH}} = 0.4 V_{\text{PP}}$, PDH modulation frequency $\nu_{\text{PDH}} = 1.56 \text{ MHz}$

ε^* [a.u.]	ϕ [rad]	σ_{PDH}	$\mathcal{S}(\sigma_{\text{PDH}})$	$\sigma_{\text{PDH,l}}$	$\mathcal{S}(\sigma_{\text{PDH,l}})$	σ_{ref}	$\mathcal{S}(\sigma_{\text{ref}})$	$\Delta\varphi$	$\mathcal{S}(\Delta\varphi)$	σ_{res}	$\mathcal{S}(\sigma_{\text{res}})$	Challenger [mrad ²]
-300	0.68	43.53	2.89	44.22	1.31	127.61	0.73	174.38	1.21	32.53	0.54	6548
-200	0.58	43.35	1.79	43.66	0.83	213.93	3.03	290.42	4.02	59.64	1.36	
-100	0.49	63.78	5.45	67.44	1.83	506.7	5.39	684.67	6.98	148.97	2.58	
100	-0.68	26.37	2.21	26.91	0.5	249.57	0.74	337.93	1.16	71.44	1.88	
200	-0.75	46.06	3.27	49.39	1.14	128.44	1.31	174.74	1.37	23.75	1.28	
300	-0.81	40.8	2.03	41.51	0.7	125.19	1.33	170.8	1.6	32.71	1.71	
-200	0.58			50.14	5.75	232.03	14.0					

Table A.8: Experimental results for PDH modulation amplitude $A_{\text{PDH}} = 0.2 V_{\text{PP}}$, PDH modulation frequency $\nu_{\text{PDH}} = 3.13 \text{ MHz}$

ε^* [a.u.]	ϕ [rad]	σ_{PDH}	$\mathcal{S}(\sigma_{\text{PDH}})$	$\sigma_{\text{PDH,l}}$	$\mathcal{S}(\sigma_{\text{PDH,l}})$	σ_{ref}	$\mathcal{S}(\sigma_{\text{ref}})$	$\Delta\varphi$	$\mathcal{S}(\Delta\varphi)$	σ_{res}	$\mathcal{S}(\sigma_{\text{res}})$	Challenger [mrad ²]
-400	0.54	50.9	2.5	50.18	1.03	457.92	5.51	631.29	7.34	102.51	3.85	8641
-300	0.49	34.07	3.02	36.1	0.66	872.16	7.82	1200.15	11.8	199.09	1.82	
-200	0.46	29.03	1.78	29.26	0.58	434.95	2.36	597.01	2.44	103.86	2.48	
-100	0.39	34.45	2.27	35.84	0.76	201.78	1.67	276.41	2.45	49.74	0.54	
100	-0.71	43.45	2.92	43.92	1.24	151.95	1.18	208.24	1.46	37.12	0.86	
200	-0.75	21.58	1.65	22.11	0.54	172.69	1.23	237.59	1.75	39.71	1.29	
300	-0.79	82.67	5.89	82.63	1.26	238.24	2.1	237.66	2.82	55.05	1.07	5422
400	-0.83	27.8	1.94	29.58	0.33	134.92	1.85	185.91	2.69	30.12	0.36	
500	-0.88	51.79	5.36	54.13	1.55	166.61	0.81	229.92	1.3	36.21	0.79	
-200	0.46			41.04	6.77	449	13.55					

Table A.9: Experimental results for PDH modulation amplitude $A_{\text{PDH}} = 0.3 V_{\text{PP}}$, PDH modulation frequency $\nu_{\text{PDH}} = 3.13 \text{ MHz}$

ε^* [a.u.]	ϕ [rad]	σ_{PDH}	$\mathcal{S}(\sigma_{\text{PDH}})$	$\sigma_{\text{PDH,l}}$	$\mathcal{S}(\sigma_{\text{PDH,l}})$	σ_{ref}	$\mathcal{S}(\sigma_{\text{ref}})$	$\Delta\varphi$	$\mathcal{S}(\Delta\varphi)$	σ_{res}	$\mathcal{S}(\sigma_{\text{res}})$	Challenger [mrad ²]
-600	0.61	48.12	2.35	51.04	0.87	449.73	18.23	622.56	25.44	90.98	2.72	
-500	0.56	42.15	5.84	44.19	0.83	413.87	4.17	572.72	6.23	85.52	1.41	
-400	0.52	33.34	2.12	33.68	1.05	8003.43	1060.52	11069.88	1477.35	1654.19	166.46	
-300	0.49	29.17	2.91	30.8	0.5	1058.93	4.87	1460.57	8.41	232.23	7.18	
-200	0.44	43.98	4.85	43.71	0.94	269.26	0.97	371.15	1.56	59.97	1.88	
-100	0.42	23.73	1.52	24.47	0.56	229.04	2.42	315.13	3.32	52.53	1.54	
100	-0.64	45.6	3.03	46.78	1.15	324.74	1.87	444.04	3.53	82.11	1.82	
200	-0.69	37.63	2.52	38.08	0.36	480.09	3.17	662.14	4.18	105.44	2.87	
300	-0.72	27.54	1.44	28.7	0.69	230.14	2.24	317.6	3.25	49.77	0.89	
400	-0.75	25.84	2.88	26.88	0.89	263.58	1.45	364.3	2.04	55	1.63	
500	-0.78	33.57	1.96	33.52	0.6	299.22	1.78	413.79	2.43	62.41	0.96	
600	-0.82	29.88	2.27	30.64	0.61	216	0.73	298.92	1.07	44.01	0.69	
700	-0.85	32.09	3.42	32.58	0.28	206.02	0.95	285.37	1.49	41.28	0.39	10078
-300	0.49			45.28	7.62	1072.04	11.6					

Table A.10: Experimental results for PDH modulation amplitude $A_{\text{PDH}} = 0.4 V_{\text{PP}}$, PDH modulation frequency $\nu_{\text{PDH}} = 3.13 \text{ MHz}$

Appendix B

Specifications

Laser NKT Photonics: Koheras Basik Module Fiber laser, Model: K82-152-13, SNR: 60 dB, Wavelength: 1550.12 nm, Linewidth: <100 Hz, Maximum output power: 200 mW, Piezo tuning: 0.1 pm/V @ 100 Hz [24]

Mach-Zehnder Modulator iXblue MX-LN-10, Bandwidth: 12 GHz, $V_{\pi,RF}$ @ 50 kHz: 5.5 V, $V_{\pi,DC}$: 6.5 V, Extinction ratio: 22 dB, Insertion loss: 3.5 dB [31]

Intra-cavity Phase Modulator EOspace Ultra-Low V_{π} phase modulator, 3 dB Bandwidth: 25 GHz, $V_{\pi,RF}$ @ 1 GHz: 2.7 V, Optical return loss: 50 dB, Insertion loss: 4 dB [1]

Arbitrary Wave Generator NI PXI-5422, 16 bits 200 MSamples/s, Bandwidth: 80 MHz [37]

Photodiodes TTI TIA-525, Bandwidth: 120 MHz [43]

Digitizer NI PXI-5124, 12 bits, 200 MSamples/s, Bandwidth: 150 MHz [36]

Band pass filter Finisar WaveShaper 4000S, Operating frequency range: 191.250 THz to 196.275 THz (1527.4 nm to 1567.5 nm), Insertion loss: 4.5 to 6.5 dB, Filter Bandwidth: 10 GHz-5 THz [49]

Boost Optical Amplifier Thorlabs BOA 1004P SOA, Wavelength range: 1530-1570 nm, Output power: 15 dBm, Gain: 27 dB [10]

Intra-cavity Erbium-Doped Fibre Amplifier Keopsys CEFA-C-BO-HP-PM, Wavelength range: 1540-1565 nm, Output power: 27 dBm, Input power range: 5-15 dBm [11]

Digilock Toptica Digilock 110, PDH frequencies: 1.56 to 25 MHz, Lock-In Amplification frequencies: 12 Hz to 781 kHz [13]

PDH Phase Modulator iXblue MPZ-LN-10-00-PP-FAFA, 3 dB Bandwidth: 16.3 GHz, $V_{\pi,RF}$ @ 50 kHz: 6.75 V, Optical return loss: 45 dB, Insertion loss: 3 dB [30]

Pre-amp Erbium-Doped Fibre Amplifier Pritel PMFA-15, Wavelength range: 1530-1565 nm, Output power: 15 dBm, Input power range: -30 to 10 dBm [35]

Acronyms

AWG	Arbitrary Wave Generator 30, 65
EDFA	Erbium-Doped Fibre Amplifier 31, 32, 38, 65
ESN	Echo State Network 9, 11, 17
FP	Fabry-Perot 26–28, 32
FSR	Free Spectral Range 21, 26, 27, 29, 35, 36, 43, 46
ML	Machine Learning 9, 10, 12, 13
MZM	Mach-Zehnder Modulator 16, 21, 30, 31, 45, 55, 65
NARMA	Nonlinear Auto-Regressive Moving Average 17, 18
NMSE	Normalised Mean Square Error 13, 18, 22
NN	Neural Network 9, 10, 14, 16, 55
PD	Photodiode 21, 34, 35, 40, 42, 44, 65
PDH	Pound-Drever-Hall 29–31, 39–47, 49–53, 56–65
PID	Proportional-Integral-Derivative 29, 40–44, 46, 53, 56
PM	Phase Modulator 20–24, 29–33, 36, 40–42, 55, 56, 65
PRC	Photonic Reservoir Computing 13–16, 20, 21, 30, 55
RC	Reservoir Computer 9–17, 19–22, 29, 45, 46, 51–53, 55, 56
RC	Reservoir Computing 9, 11, 17, 53, 55
RNN	Recurrent Neural Network 9, 55
RTT	Round Trip Time 14, 21
SER	Signal Error Rate 17, 22
SNR	Signal to Noise Ratio 17, 19, 31, 45
SOA	Semiconductor Optical Amplifier 13, 16, 31, 65
TDM	Time Division Multiplexing 9, 13–16, 20
WDM	Wavelength Division Multiplexing 20, 21, 30, 55

Bibliography

- [1] A. Akrout et al. “Parallel photonic reservoir computing using frequency multiplexing of neurons”. In: (2016).
- [2] Ivan Amato. “Speculating in precious computronium: a new computer embodies an architecture that-to its creators-mimics the structure and dynamics of physical reality”. In: *Science* 253.5022 (1991), pp. 856–858.
- [3] Piotr Antonik et al. “Online Training of an Opto-Electronic Reservoir Computer Applied to Real-Time Channel Equalization”. In: *IEEE Transactions on Neural Networks and Learning Systems* 28.11 (Nov. 2017), pp. 2686–2698. URL: <https://doi.org/10.1109/tnnls.2016.2598655>.
- [4] A. Bernal, S. Fok, and R. Pidaparthi. “Financial Market Time Series Prediction with Recurrent Neural Networks”. In: (2012). URL: <http://citeseerx.ist.psu.edu/viewdoc/download?doi=10.1.1.278.3606&rep=rep1&type=pdf>.
- [5] Christopher Bishop. *Pattern recognition and machine learning*. New York: Springer, 2006. ISBN: 978-0387-31073-2.
- [6] Eric Black. “Notes on pound-drever-hall technique”. In: *LIGO Technical notes* (1998).
- [7] Volkmar Brückner. “To the use of Sellmeier formula”. In: (May 2014).
- [8] Daniel Brunner and Ingo Fischer. “Reconfigurable semiconductor laser networks based on diffractive coupling”. In: *Optics Letters* 40.16 (Aug. 2015), p. 3854. URL: <https://doi.org/10.1364/ol.40.003854>.
- [9] H. John Caulfield and Shlomi Dolev. “Why future supercomputing requires optics”. In: *Nature Photonics* 4.5 (May 2010), pp. 261–263. URL: <https://doi.org/10.1038/nphoton.2010.94>.
- [10] *C-Band Booster Optical Amplifier BOA 1004P PM Fiber*. Thorlabs. Apr. 2019. URL: <https://www.thorlabs.com/drawings/fd6c1557aa47f7d3-CEC70D3E-9A30-0668-D7B015F14871FFBB/BOA1004P-SpecSheet.pdf>.
- [11] *CEFA-C-BO-HP Series*. v2.5. Keopsys. URL: <http://www.sun-ins.com/lineup3/keopsys/pdf/CEFA-C-BO-HP.pdf>.
- [12] Antoine Dejonckheere et al. “All-optical reservoir computer based on saturation of absorption”. In: *Optics Express* 22.9 (Apr. 2014), p. 10868. URL: <https://doi.org/10.1364/oe.22.010868>.
- [13] *Digilock 110 Feedback Controlyzer Manual*. v05. Toptica. May 2013. URL: https://www.toptica.com/fileadmin/Editors_English/03_products/03_tunable_diode_lasers/04_control_electronics/02_laser_locking_electronics/DigiLock_110/toptica_Digilock_Manual.pdf.
- [14] RWP Drever et al. “Laser phase and frequency stabilization using an optical resonator”. In: *Applied Physics B* 31.2 (1983), pp. 97–105.

- [15] François Duport et al. “Fully analogue photonic reservoir computer”. In: *Scientific Reports* 6.1 (Mar. 2016). URL: <https://doi.org/10.1038/srep22381>.
- [16] Chrisantha Fernando and Sampsa Sojakka. “Pattern Recognition in a Bucket”. In: *Advances in Artificial Life*. Springer Berlin Heidelberg, 2003, pp. 588–597. URL: https://doi.org/10.1007/978-3-540-39432-7_63.
- [17] Gene Franklin. *Feedback control of dynamic systems*. Boston: Pearson, 2015. ISBN: 9780133496598.
- [18] Alireza Goudarzi et al. “A Comparative Study of Reservoir Computing for Temporal Signal Processing”. In: *CoRR* abs/1401.2224 (2014).
- [19] H. Jaeger. “Harnessing Nonlinearity: Predicting Chaotic Systems and Saving Energy in Wireless Communication”. In: *Science* 304.5667 (Apr. 2004), pp. 78–80. URL: <https://doi.org/10.1126/science.1091277>.
- [20] H. Jaeger. *The "echo state" approach to analysing and training recurrent neural networks*. 2001.
- [21] Herbert Jaeger. “Adaptive Nonlinear System Identification with Echo State Networks”. In: *Proceedings of the 15th International Conference on Neural Information Processing Systems*. NIPS’02. Cambridge, MA, USA: MIT Press, 2002, pp. 609–616. URL: <http://dl.acm.org/citation.cfm?id=2968618.2968694>.
- [22] Herbert Jaeger. “Tutorial on training recurrent neural networks, covering BPPT, RTRL, EKF and the echo state network approach”. In: *GMD-Forschungszentrum Informationstechnik, 2002*. 5 (Jan. 2002).
- [23] Herbert Jaeger et al. “Optimization and applications of echo state networks with leaky- integrator neurons”. In: *Neural Networks* 20.3 (Apr. 2007), pp. 335–352. URL: <https://doi.org/10.1016/j.neunet.2007.04.016>.
- [24] *Koheras Adjustik E15*. NKT Photonics. URL: <https://www.nktphotonics.com/wp-content/uploads/sites/3/2015/04/koheras-adjustik-e15.pdf?1552493817>.
- [25] Rolf Landauer. “Information is Physical”. In: *Physics Today* 44.5 (May 1991), pp. 23–29. URL: <https://doi.org/10.1063/1.881299>.
- [26] M. Lukoševičius and H. Jaeger. “Reservoir computing approaches to recurrent neural network training”. In: *Computer Science Review* 3.3 (Aug. 2009), pp. 127–149. URL: <https://doi.org/10.1016/j.cosrev.2009.03.005>.
- [27] M. Lukoševičius, M. Jaeger, and B. Schrauwen. “Reservoir Computing Trends”. In: *KI - Künstliche Intelligenz* 26.4 (May 2012), pp. 365–371. URL: <https://doi.org/10.1007/s13218-012-0204-5>.
- [28] IH Malitson. “Interspecimen comparison of the refractive index of fused silica”. In: *Josa* 55.10 (1965), pp. 1205–1209.
- [29] Marvin Minsky. *Perceptrons; an introduction to computational geometry*. Cambridge, Mass: MIT Press, 1969. ISBN: 9780262130431.
- [30] *MPX and MPZ Serires Low frequencies to 40 GHz Phase Modulators*. iXblue Photonics. URL: <https://photonics.ixblue.com/sites/default/files/2018-12/C-Band%20Phase%20Modulators.pdf>.
- [31] *MX-LN series, 1550 nm band Intensity Modulators*. iXblue Photonics. URL: <https://photonics.ixblue.com/sites/default/files/2018-12/NRZ%20DPSK%20RZ%20Intensity%20Modulators.pdf>.

- [32] M Nickerson. “A review of pound drever hall laser frequency locking”. In: *JILA, University of Colorado and Nist* ().
- [33] Y. Paquot et al. “Optoelectronic Reservoir Computing”. In: *Scientific Reports* 2.1 (Feb. 2012). URL: <https://doi.org/10.1038/srep00287>.
- [34] A. Perot and Charles Fabry. “On the Application of Interference Phenomena to the Solution of Various Problems of Spectroscopy and Metrology”. In: *The Astrophysical Journal* 9 (Feb. 1899), p. 87. URL: <https://doi.org/10.1086/140557>.
- [35] *PMFA Series Polarization Maintaining Optical Fiber Amplifiers*. Pritel. URL: https://www.pritel.com/pdfs/PMFA_R10A.pdf.
- [36] *PXI-5124*. National Instruments. Mar. 2019. URL: <http://www.ni.com/pdf/manuals/3711351.pdf>.
- [37] *PXI-5422*. National Instruments. Nov. 2018. URL: <http://www.ni.com/pdf/manuals/371400f.pdf>.
- [38] F. Rosenblatt. “The Perceptron: A Probabilistic Model for Information Storage and Organization in The Brain”. In: *Psychological Review* (1958), pp. 65–386.
- [39] Stuart Russell. *Artificial intelligence : a modern approach*. Upper Saddle River, New Jersey: Prentice Hall, 2010. ISBN: 978-0-13-604259-4.
- [40] Guy Van der Sande, Daniel Brunner, and Miguel C. Soriano. “Advances in photonic reservoir computing”. In: *Nanophotonics* 6.3 (Jan. 2017). URL: <https://doi.org/10.1515/nanoph-2016-0132>.
- [41] Benjamin Schrauwen, David Verstraeten, and Jan Campenhout. “An overview of reservoir computing: Theory, applications and implementations”. In: Jan. 2007, pp. 471–482.
- [42] Claude Elwood Shannon. “A mathematical theory of communication”. In: *Bell system technical journal* 27.3 (1948), pp. 379–423.
- [43] *TIA-525 Optical/Electrical Converter*. Terahertz Technologies Inc. Apr. 2011. URL: <http://www.terahertztechnologies.com/pdfmanuals/TIA525-Manual.pdf>.
- [44] Fabian Triefenbach et al. “Phoneme Recognition with Large Hierarchical Reservoirs”. In: *Advances in Neural Information Processing Systems 23*. Ed. by J. D. Lafferty et al. Curran Associates, Inc., 2010, pp. 2307–2315. URL: <http://papers.nips.cc/paper/4056-phoneme-recognition-with-large-hierarchical-reservoirs.pdf>.
- [45] Kristof Vandoorne et al. “Experimental demonstration of reservoir computing on a silicon photonics chip”. In: *Nature Communications* 5.1 (Mar. 2014). URL: <https://doi.org/10.1038/ncomms4541>.
- [46] Kristof Vandoorne et al. “Toward optical signal processing using Photonic Reservoir Computing”. In: *Optics Express* 16.15 (July 2008), p. 11182. URL: <https://doi.org/10.1364/oe.16.011182>.
- [47] D. Verstraeten, B. Schrauwen, and D. Stroobandt. “Reservoir-based techniques for speech recognition”. In: *The 2006 IEEE International Joint Conference on Neural Network Proceedings*. IEEE, 2006. URL: <https://doi.org/10.1109/ijcnn.2006.246804>.
- [48] Quentin Vinckier et al. “High-performance photonic reservoir computer based on a coherently driven passive cavity”. In: *Optica* 2.5 (Apr. 2015), p. 438. URL: <https://doi.org/10.1364/optica.2.000438>.

- [49] *WaveShaper 4000S Multiport Optical Processor*. Finisar. Nov. 2014. URL: https://www.finisar.com/sites/default/files/downloads/waveshaper_4000s_product_brief_11_14.pdf.